How to cite: *Angew. Chem. Int. Ed.* **2021**, *60*, 22865–22870
International Edition: doi.org/10.1002/anie.202107963
German Edition: doi.org/10.1002/ange.202107963

Gas Separation **Hot Paper**

Interpenetration Symmetry Control Within Ultramicroporous Robust Boron Cluster Hybrid MOFs for Benchmark Purification of Acetylene from Carbon Dioxide

Lingyao Wang[+], Wanqi Sun[+], Yuanbin Zhang, Nuo Xu, Rajamani Krishna, Jianbo Hu, Yunjia Jiang, Yabing He, and Huabin Xing**

Abstract: *The separation of C_2H_2/CO_2 is an important process in industry but challenged by the trade-off of capacity and selectivity owning to their similar physical properties and identical kinetic molecular size. We report the first example of symmetrically interpenetrated dodecaborate pillared MOF, ZNU-1, for benchmark selective separation of C_2H_2 from CO_2 with a high C_2H_2 capacity of 76.3 $cm^3 g^{-1}$ and record C_2H_2/CO_2 selectivity of 56.6 (298 K, 1 bar) among all the robust porous materials without open metal sites. Single crystal structure analysis and modeling indicated that the interpenetration shifting from asymmetric to symmetric mode provided optimal pore chemistry with ideal synergistic "2+2" dihydrogen bonding sites for tight C_2H_2 trapping. The exceptional separation performance was further evidenced by simulated and experimental breakthroughs with excellent recyclability and high productivity (2.4 mol kg^{-1}) of 99.5 % purity C_2H_2 during stepped desorption process.*

Introduction

Acetylene (C_2H_2) is an important precursor chemical for the synthesis of various organic chemicals and polymers. It is mainly produced from the stream cracking of hydrocarbons or partial combustion of natural gas, in which carbon dioxide (CO_2) coexists unavoidably as a contaminant and needs to be removed to produce C_2H_2 in high purity (> 99 %).[1] Since C_2H_2 and CO_2 molecules have very similar physical properties (boiling points: C_2H_2, 189.3 K; CO_2, 194.7 K) and identical kinetic molecular size (3.3 Å), the C_2H_2/CO_2 separation represents one of the most difficult and challenging chemical separations.[2] Current technology for the separation and purification of C_2H_2 from other gases is generally dependent on cryogenic distillation or solvent extraction, which are either cost-/energy-intensive or associated with pollution. In this context, physisorptive separation using porous solid adsorbents has attracted particular interest based on the lower cost and energy consumption.[3]

Metal–organic frameworks (MOFs), or porous coordination polymers (PCPs), have emerged as a new class of promising porous materials for gas separation due to their powerful predictability and tunability on pore size/shape and functionality.[4] These advanced characteristics have allowed the prospective design of target materials with desirable properties for specific gas separations.[5] In this regard, several microporous materials that can selectively capture C_2H_2 from CO_2 have been reported.[6] However, those exhibiting a high C_2H_2 capacity and high selectivity over CO_2 are very rare. Two leading materials with size sieving effect are UTSA-300a and CPL-1-NH_2. Both materials are flexible and show lower gate opening pressure for C_2H_2 and higher gate opening pressure for CO_2. However, the uptake of C_2H_2 on UTSA-300a (68.9 $cm^3 g^{-1}$)[6a] and CPL-1-NH_2 (41.2 $cm^3 g^{-1}$)[6b] under 1 bar and 298 K is relatively modest, and co-adsorption of CO_2 is inevitable after the pore expansion induced by C_2H_2 in practical breakthrough experiments. Other two porous materials with high IAST selectivity (> 50) are ATC-Cu[6c] and Cu@UiO-66-$(COOH)_2$.[6d] Both materials contain coordinately unsaturated metal sites and exhibit ultrahigh C_2H_2 adsorption heats (79.1 and 74.5 kJ mol^{-1}). Such high values are close to those from chemical adsorption, rendering the recovery of C_2H_2 and regeneration of the adsorbents difficult and energy-intensive. To the best of our knowledge, none have discovered a robust porous material with modestly high adsorption heats (< 60 kJ mol^{-1}) but quite high capacity (> 70 $m^3 g^{-1}$) and selectivity (> 50) under ambient conditions. To realize it, unique binding sites should be deliberately designed.

Recently, Zaworotko et al. reported that halogen-C_2H_2 binding in ultramicroporous MOFs can be utilized to realize high C_2H_2/CO_2 separation selectivity (16.9).[7] Compared to fluorinated anions (SiF_6^{2-}, TiF_6^{2-}) that form strong interaction to both C_2H_2 and CO_2, less negatively charged halogen atoms show enhanced discriminatory effects for C_2H_2 and CO_2. Similarly, electronegative B-$H^{\delta-}$ units from *closo*-dodecaborate anions have been demonstrated to form strong hydride-proton dihydrogen bonding with C_2H_2 ($\Delta E = -40.2$ kJ mol^{-1}, Scheme 1) but much weaker electrostatics with CO_2 ($\Delta E =$

[*] Dr. L. Wang,[+] W. Sun,[+] Dr. Y. Zhang, N. Xu, Y. Jiang, Prof. Y. He
Key Laboratory of the Ministry of Education for Advanced Catalysis Materials, College of Chemistry and Life Sciences
Zhejiang Normal University, Jinhua 321004 (P. R. China)
E-mail: ybzhang@zjnu.edu.cn
Dr. J. Hu, Prof. H. Xing
China Key laboratory of Biomass Chemical Engineering of Ministry of Education, College of Chemical and Biological Engineering
Zhejiang University, Hangzhou 310027 (P. R. China)
E-mail: xinghb@zju.edu.cn
Prof. R. Krishna
Van't Hoff Institute for Molecular Sciences, University of Amsterdam
Science Park 904, 1098 XH Amsterdam (Netherlands)
[+] These authors contributed equally to this work.
Supporting information and the ORCID identification number(s) for the author(s) of this article can be found under: https://doi.org/10.1002/anie.202107963.

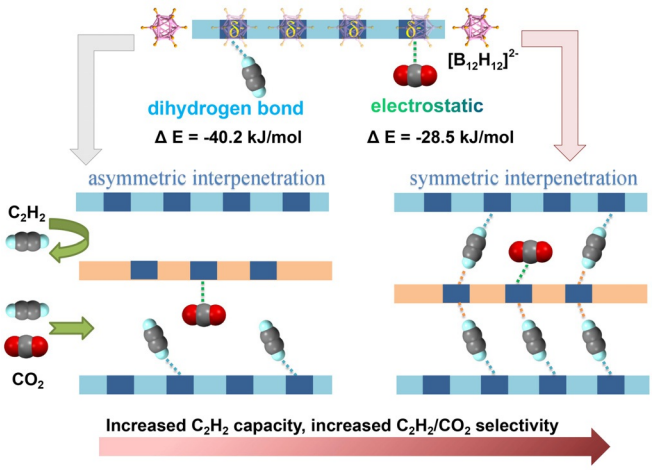

Scheme 1. Illustration of tuning the asymmetric interpenetration to symmetric interpenetration for enhanced C_2H_2/CO_2 separation.

$-28.5\ kJ\,mol^{-1}$, Scheme 1), leading to high C_2H_2/CO_2 separation selectivity in ultramicroporous BSF-3 (16.3)[8a] and BSF-4 (9.8).[8b] However, It need to be noted that all the reported interpenetrated boron cluster hybrid supramolecular metal-organic frameworks (BSFs) are asymmetrically interpenetrated (Scheme 1, left), no matter what boron clusters or organic linkers are used.[8] This is probably due to the symmetry mismatch of the *closo*-dodecaborate pillar and the M_4L_4 (Figure 1 A, B; M = metal ion, L = organic linker) grid as well as the formation of particular $B{-}H^{\delta-}{\cdots}H^{\delta+}{-}C_{Py}$ interactions between the dodecaborates and some pyridyl linkers. Although these BSFs have already shown selectivity superior to most of the porous material, yet still far from the expectation value ($S > 50$) for the production of high purity C_2H_2 (> 99 %) during desorption process. In theory, symmetrical interpenetration in the ultramicroporous BSF materials is advantageous for enhancing C_2H_2 capacity and C_2H_2/CO_2 selectivity as this not only provides more space for gas accommodation but also enables strong trap of acetylene by synergistic dihydrogen interactions (Scheme 1, right). Nonetheless, no strategies can be followed in the references for rationally manipulating the interpenetration symmetry, despite several reports on control of the interpenetration degree, e.g., structural tuning between non-interpenetrated and 2-fold interpenetrated by changing the synthetic temperature or solvents.[9] In brief, symmetrically interpenetrated BSFs are theoretically promising to tackle the trade-off between the C_2H_2 capacity and C_2H_2/CO_2 selectivity with low energy demand but extraordinarily challenging in the bottom-up design and synthesis.

Herein, we would like to report the discovery of the first example of symmetrically interpenetrated BSF material termed as ZNU-1 (ZNU = Zhejiang Normal University) with the composition of $CuB_{12}H_{12}(dpe)_2$ (dpe = 1,2-di(4-pyridyl)-ethylene). The structure of ZNU-1 was confirmed by single crystal diffraction analysis. Gas adsorption studies indicated that ZNU-1 exhibited highly acetylene-selective adsorption with high capacity ($76.3\ cm^3\,g^{-1}$) and selectivity (56.6) over CO_2. Notably, the C_2H_2 adsorption heat (Q_{st}) of $54\ kJ\,mol^{-1}$ is not ultrahigh, which allows the facile regeneration of the adsorbent and recovery of the adsorbed C_2H_2. Notably, the combination of large C_2H_2 capacity ($> 70\ cm^3\,g^{-1}$), high C_2H_2/CO_2 selecticity (> 50) and modestly high Q_{st} ($< 60\ kJ\,mol^{-1}$) has been realized for the first time. The effective separation of mixed C_2H_2/CO_2 gases was further demonstrated by column-

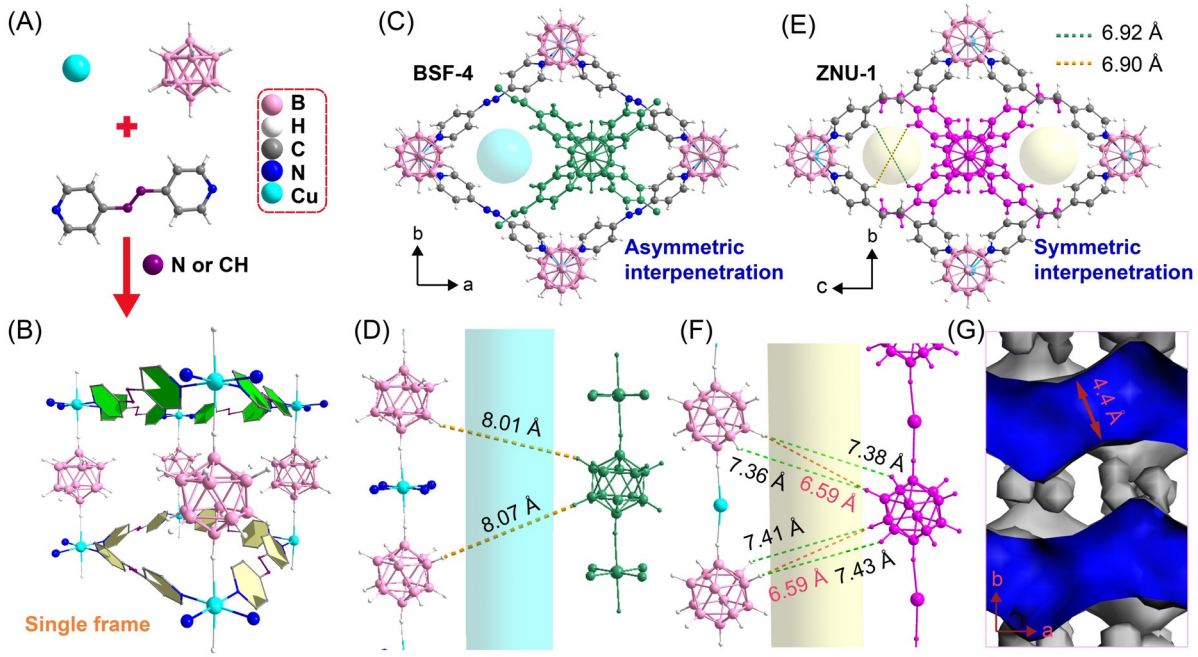

Figure 1. Altering of interpenetration symmetry in BSF materials by choosing slightly different dipyridyl ligands. Despite featuring similar single frame (A, B), BSF-4 (C, D) is asymmetrically interpenetrated while ZNU-1 (E, F, G) is symmetrically interpenetrated. All displayed structures are based on X-ray crystallography.

breakthrough experiments employing equimolar binary mixtures with good recyclability. During desorption process, 2.9 mol kg^{-1} of 98% pure C_2H_2 or 2.4 mol kg^{-1} > 99.5% pure C_2H_2 can be recovered from the column by stepped Ar purge/vacuum swing process. Modelling studies revealed the high acetylene capacity and benchmark selectivity of C_2H_2/CO_2 were attributed to the unique symmetric interpenetration that provides suitable pore chemistry and size with ideal "2+2" dihydrogen bonding interaction sites to tightly trap C_2H_2.

Results and Discussion

Single crystals of ZNU-1 were cultivated by layering a MeOH solution of dpe onto an aqueous solution of $Cu[B_{12}H_{12}]$. X-ray structural analysis of ZNU-1 revealed that it crystallizes in a three-dimensional (3D) framework in the orthorhombic space group Pbcn, different from BSF-4 ($CuB_{12}H_{12}(apy)_2$, apy = 4,4′-azopyridine) with monoclinic space group *C*2/*c*. ZNU-1 and BSF-4 feature nearly identical single frame (Figure 1A, B) due to the similar length and shape of organic linkers (9.0 Å for apy and 9.3 Å for dpe). Multiple $B{-}H^{\delta-}{\cdots}H^{\delta+}{-}C_{Py}$ dihydrogen bonds (2.17–2.40 Å) between the $[B_{12}H_{12}]^{2-}$ anions and pyridyl groups can be observed (Figure S4). Notably, BSF-4 is asymmetrically interpenetrated (Figure 1C) as other BSFs (Figure S6) while ZNU-1 features symmetric interpenetration (Figure 1E). Therefore, only the largest pore is accessible in BSF-4 while two pores are useful in ZNU-1. The closest distances of B-H units in BSF-4 are between 8.01–8.07 Å while those for ZNU-1 were suited between 6.59–7.38 Å. Considering the H···H distance of 3.37 Å in C_2H_2 as well as the definition of dihydrogen bonding ($H^{\delta-}{\cdots}H^{\delta+}$ distance < 2.4 Å), DFT calculation predicted that the H(B)···H(B) distances between the opposite dodecaborates should be less than 7.7 Å to forming synergistic $B{-}H^{\delta-}{\cdots}H^{\delta+}{-}C{\equiv}C{-}H^{\delta+}{\cdots}H^{\delta-}{-}B$ dihydrogen bonding with C_2H_2. Therefore, ZNU-1 was a good candidate as a C_2H_2 trap while BSF-4 failed. The pore size determined using a probe of 1.2 Å by PLATON was ≈4.4 Å (Figure 1G, S3), close to the kinetic diameter of C_2H_2 (3.3 Å).

To confirm the permanent porosity after solvent removal, N_2 gas adsorption experiments at 77 K were conducted, which indicated the microporous character of ZNU-1 with a BET surface area of 532 $m^2 g^{-1}$ and a pore volume of 0.20 $cm^3 g^{-1}$, consistent with the calculated values of 545 $m^2 g^{-1}$ and 0.204 $cm^3 g^{-1}$ from single crystal data.

Then, single component C_2H_2 and CO_2 adsorption measurements at 298 K were conducted. At 1.0 bar, the C_2H_2 and CO_2 uptakes were 76.3 and 38.1 mL g^{-1} for ZNU-1 (Figure 2A). The C_2H_2 uptake on ZNU-1 was 43% higher than that of BSF-4 while both CO_2 uptakes were similar (Figure 2A). Notably, ZNU-1 adsorbed a large amount of C_2H_2 at low pressure regions. The uptakes under 0.01 and 0.1 bar are 1.22 and 2.52 mmol g^{-1}, 2.3 and 1.75 folds of those on BSF-4, respectively (Figure 2F). These uptake capacities are also the highest among all the reported BSFs (Figure 2F). Moreover, the C_2H_2/CO_2 uptake ratio in ZNU-1 at 0.01 bar was as high as 24, superior to many leading materials such as UTSA-74a (14.5),[2b] JCM-1 (4.6),[1b] NKMOF-1-Ni (4.6)[10] and FJU-90 (3.5).[11] The selectivity for equimolar C_2H_2/CO_2 gas mixtures on ZNU-1 and BSF-4 at 298 K were calculated using ideal adsorbed solution theory (IAST) after fitting isotherms to the dual-site Langmuir equation with excellent accuracy (Table S3, $R^2 > 0.998$). Figure 2B revealed that the selectivity for equimolar C_2H_2/CO_2 at 298 K and 1.0 bar were 56.6 and 9.8 for ZNU-1 and BSF-4 respectively. Compared to other BSFs and benchmark anion hybrid MOFs, ZNU-1 exhibited remarkably increased IAST selectivity, which is also higher than ATC-Cu (53.6),[6c] ZJU-74a (36.5),[12] etc, and the highest among all the robust materials without open metal sites

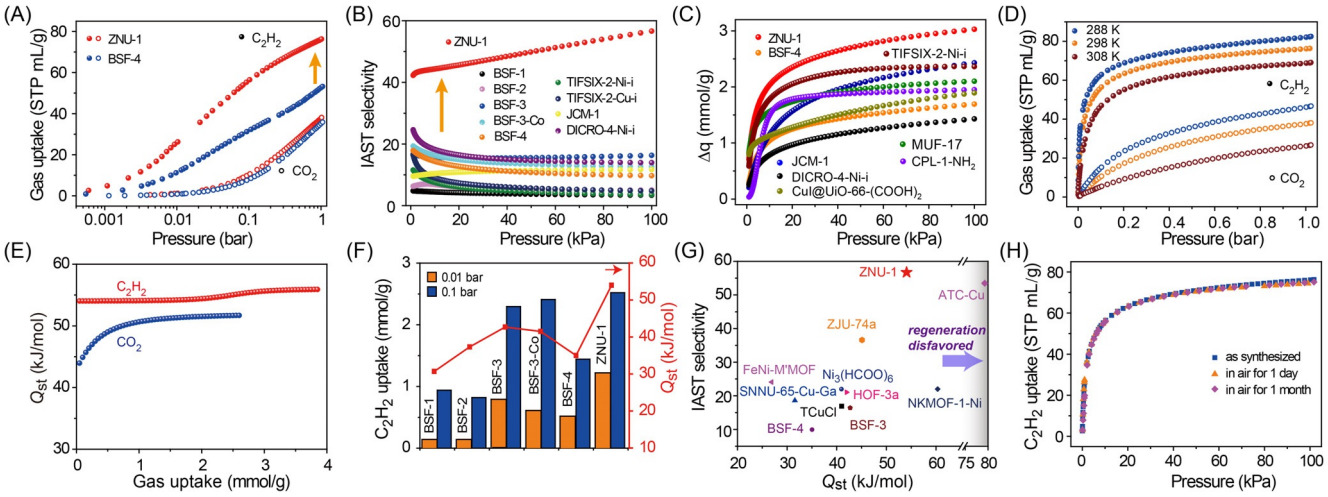

Figure 2. A) C_2H_2 and CO_2 adsorption isotherms for ZNU-1 and BSF-4 at 298 K; B) IAST adsorption selectivity comparison among best-performing anion hybrid MOFs toward a 1:1 mixture of C_2H_2/CO_2; C) comparison of ZNU-1 capacity difference ($\Delta q = C_2H_2$ uptake − CO_2 uptake) to adsorb C_2H_2 and CO_2 from C_2H_2/CO_2 (50/50) mixtures with reported benchmark MOFs based on IAST calculation; D) C_2H_2 and CO_2 adsorption isotherms for ZNU-1 at 288, 298, and 308 K; E) the isosteric heat of adsorption, Q_{st}, for C_2H_2 and CO_2 in ZNU-1; F) comparison of the C_2H_2 uptakes under low pressure and Q_{st} among BSFs; G) comparison of the IAST selectivity and Q_{st} among reported benchmark materials; H) repeated measurement of C_2H_2 adsorption in ZNU-1 after exposure to air.

(Figure 2G, Table S6). The static C_2H_2 and CO_2 uptake from the equimolar mixture of C_2H_2/CO_2 were calculated for ZNU-1 and other leading materials. The capacity differences (Δq) between C_2H_2 and CO_2 were compared, which showed a trend of ZNU-1 (3.03 mmol g^{-1}) > JCM-1 (2.43 mmol g^{-1}) > TIFSIX-2-Ni-i (2.36 mmol g^{-1}) > MUF-17 (2.10 mol g^{-1})[13] > CPL-1-NH_2 (1.95 mmol g^{-1}) > CuI@UiO-66-$(COOH)_2$ (1.89 mmol g^{-1}) > BSF-4 (1.69 mmol g^{-1}) > DICRO-4-Ni-i (1.43 mmol g^{-1})[14] at 100 kPa and 298 K (Figure 2C). The C_2H_2 and CO_2 adsorption isotherms on ZNU-1 were further collected at 288 K and 308 K and all revealed type I isotherms (Figure 2D). The isosteric heats of adsorption (Q_{st}) for ZNU-1 were then calculated using the Clausius-Clapeyron equation. Q_{st} values at near-zero loading for C_2H_2 and CO_2 were 54.0 and 44.0 kJ mol^{-1} (Figure 2E). The CO_2 adsorption heat was increased with the CO_2 loading probably due to the strong intermolecular interactions between close CO_2 molecules within the confined pores, but still lower than that for C_2H_2. As expected, the Q_{st} value for C_2H_2 in ZNU-1 is higher than those in BSF-4 (35.0 kJ mol^{-1}), BSF-3-Co (41.5 kJ mol^{-1}), BSF-3 (42.7 kJ mol^{-1}), BSF-2 (37.3 kJ mol^{-1}), and BSF-1 (30.7 kJ mol^{-1}) and many other well-performing porous materials (Figure 2G), but distinctly lower than those of ATC-Cu (79.1 kJ mol^{-1})[6c] and Cu@UiO-66-$(COOH)_2$ (74.5 kJ mol^{-1}).[6d] Generally speaking, this modestly high Q_{st} value of ZNU-1 not only confirms the strong affinity for C_2H_2 adsorption but also allows the easy desorption of C_2H_2 for recovery as well as the facile regeneration of the adsorbent. More importantly, ZNU-1 is less sensitive towards air exposure and retains the capacity for C_2H_2 adsorption at 1.0 bar (Figure 2H) while BSF-3 and BSF-4 lose >10% of capacity after exposure to air for 1 month.[8]

To confirm our hypothesis as well as gain more insight into the gas adsorption behavior, modeling studies using grand canonical Monte Carlo (GCMC) simulations and DFT calculations were performed. As expected, C_2H_2 molecules were only adsorbed in the largest pore in BSF-4 but in both pores in ZNU-1 (Figure S28). The optimized adsorption configuration of C_2H_2@ZNU-1 showed extraordinary "2+2" synergistic B–$H^{\delta-}$···$H^{\delta+}$–C≡C–$H^{\delta+}$···$H^{\delta-}$–B dihydrogen bonds with proton hydride distance of 2.183, 2.263, 2.285, and 2.397 Å (Figure 3A). The calculated bonding energy of 56.9 kJ mol^{-1} was highly consistent with the experimental adsorption heat (54.0 kJ mol^{-1}) calculated from the adsorption isotherms and remarkably higher than the calculated bonding energy from single dodecaborate (Figure S27, 40.2 kJ mol^{-1}). Such ideal dihydrogen bonding sites have never been realized in previous BSFs (Figures S29-31). In sharp contrast, CO_2 only interacted with single dodecabate anion with the $H^{\delta-}$···$C^{\delta+}$ distance of 2.609 Å and bonding energy of 37.6 kJ mol^{-1} (Figure 3B). The large bonding energy difference based on the different recognition mechanism towards C_2H_2 and CO_2 well illustrated the different gas adsorption behaviors in ZNU-1. Notably, a distinct B-H stretch (2480–2400 cm^{-1}) signal shift can be observed in IR spectra after loading of C_2H_2 gas (Figure S9), which gave direct experimental evidence of strong affinity of ZNU-1 towards C_2H_2 through B–$H^{\delta-}$···$H^{\delta+}$–C interaction.

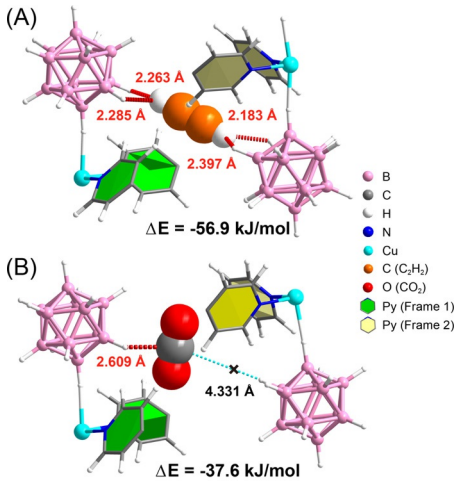

Figure 3. The DFT-D optimized adsorption configuration and bonding energy of C_2H_2 (A) and CO_2 (B) in ZNU-1.

To evaluate the feasibility of ZNU-1 for selective C_2H_2 purification from binary C_2H_2/CO_2 mixture, transient breakthrough simulations were conducted for equimolar C_2H_2/CO_2 (50/50) mixture in a column adsorption-desorption cycle.[15] The results showed that highly efficient separations could be accomplished by ZNU-1 with 2.90 mol kg^{-1} of C_2H_2 productivity (Figure 4A, B). Desorption simulations further indicated that 98% purity C_2H_2 could be recovered in a counter-current blowdown process while the purity of C_2H_2 desorbed from BSF-4 was only 90% (Figure 4C). The comparison of the dynamic separation potential Δq_{break} calculated from the breakthrough simulations also confirmed the best performance of ZNU-1 (Figure 4D), well consistent with the static separation potential Δq_{IAST} based on the adsorption isotherms. We further carried out the experimental breakthrough studies with C_2H_2/CO_2 (50/50) mixture flowed over a ZNU-1 packed column at 298 K under different flow rate. Clean separations were achieved. Figures 4E and F showed the breakthrough curves of ZNU-1 for C_2H_2/CO_2 mixture with the flow rate of 1.2 and 5 mL min^{-1}. Both experimental results were very similar with the simulations. CO_2 appeared at the outlet of the column at the beginning while C_2H_2 breakthrough occurred after ca. 226 and 58 min. The corresponding calculated C_2H_2 adsorption amount were ≈2.9 and ≈3.1 mmol g^{-1} under the flow rate of 1.2 and 5 mL min^{-1}, respectively. Both of the separation factors were calculated to be ≈49, consistent with the IAST selectivity. More breakthrough studies under different temperature, with different sample loading and cycling experiments can be found in the supporting information (Figures S21–26), which all indicated the high separation efficiency and good recyclability of ZNU-1 over 10 cycles. As C_2H_2 is the target gas that needs to be purified, the desorption process is very important to produce high purity C_2H_2. As ZNU-1 showed relatively high affinity towards C_2H_2 and much weaker affinity towards CO_2, it is possible to remove the trace CO_2 impurities from the column first and recover the high purity C_2H_2 afterwards. With this idea in mind, we designed different conditions to recover C_2H_2. A further positive finding is that almost all of the

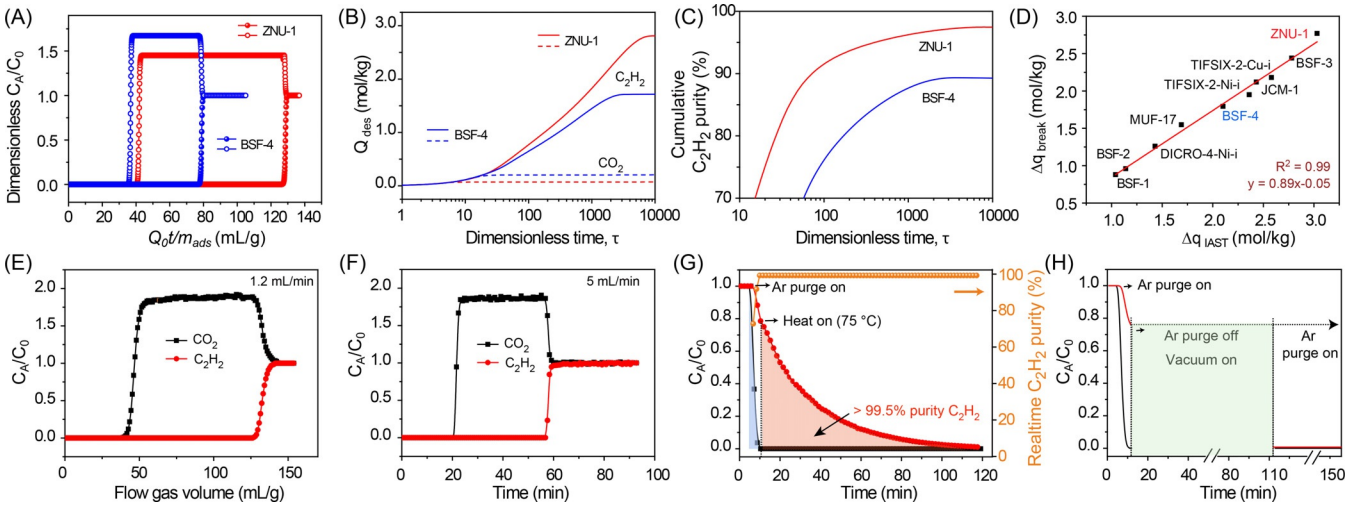

Figure 4. A) Simulated breakthrough curves of ZNU-1 and BSF-4 for C_2H_2/CO_2 (50/50) at 298 K. B) Cumulative recovery of C_2H_2 and CO_2 during simulated counter-current blowdown operations. C) Cumulative purity of C_2H_2 recovered form ZNU-1 and BSF-4 during simulated counter-current blowdown operations. D) Plots of the calculated separation potential Δq_{break} in the fixed bed with the calculated separation potential Δq_{IAST} from the static adsorption isotherms for equimolar C_2H_2/CO_2 mixture, E) The experimental column breakthrough curves of ZNU-1 for C_2H_2/CO_2 (50/50) at 298 K with a flow rate of 1.2 mL min^{-1}. F) The experimental column breakthrough curves of ZNU-1 for C_2H_2/CO_2 (50/50) at 298 K with a flow rate of 5 mL min^{-1}. G),H) Stepped desorption curves by Ar purge or vacuum.

adsorbed CO_2 could be removed within 5 min under the purge of Ar with the flow rate of 5 mL min^{-1} under room temperature. Since then, the continuing purge of Ar with increasing temperature produced high purity (> 99.5 %) C_2H_2 and the production was estimated to be ≈ 2.4 mol kg^{-1} (Figure 4G). Vacuum desorption was also tested, which indicated the high purity C_2H_2 could be completely recovered within 100 min at room temperature after blowing CO_2 out at the beginning (Figure 4H) as the subsequent Ar purge indicated nearly no C_2H_2 residue existing in the column. To the best of our knowledge, it is the first time to realize the high production (> 2 mol kg^{-1}) of high purity (> 99.5 %) C_2H_2 by a C_2H_2-selective MOF, where the key relies on the precise control of the stepped desorption process to desorb CO_2 first with the minimum loss of C_2H_2. The combination of high productivity of high purity C_2H_2, good recycling performance and facile regeneration conditions of the material renders it as a potential adsorbent for practical C_2H_2/CO_2 separation.

Conclusion

We reported the first symmetrically interpenetrated boron cluster pillared MOF, ZNU-1, for the benchmark separation of C_2H_2 and CO_2. The combination of large C_2H_2 capacity (76.3 cm^3 g^{-1}), ultrahigh C_2H_2/CO_2 selectivity (56.6) and modestly high adsorption heat (54.0 kJ mol^{-1}) for regeneration has been realized for the first time. The efficient separation of mixed C_2H_2/CO_2 gases was practically confirmed by column-breakthrough experiments employing equimolar binary mixture with good recyclability. 2.8 mol kg^{-1} of 98 % pure C_2H_2 or 2.4 mol kg^{-1} > 99.5 % pure C_2H_2 can be recovered by stepped desorption from the column by stepped Ar purge or vacuum pump. DFT calculation indicated C_2H_2 molecules were trapped by extraordinary synergistic "2+2" dihydrogen bonds within the well-suited pore due to the symmetric interpenetration. Generally, our work demonstrates the importance of the boron cluster functionality and the control of interpenetration symmetry for constructing synergistic interaction sites in porous materials for gas separation.

Acknowledgements

This work was supported by the Natural Science Foundation of China (No. 21908193, 21938011, 21725603), and the Research Computing Center in College of Chemical and Biological Engineering at Zhejiang University. We thank Prof. J. Duan (Nanjin Tech University) for the technical assistance with the breakthrough equipment and Prof. D. Wang (Zhejiang Normal University) for allowing us to use her gas adsorption equipment.

Conflict of Interest

The authors declare no conflict of interest.

Keywords: acetylene adsorption · boron clusters · C_2H_2/CO_2 separation · synergistic interaction · ultramicroporous MOFs

[1] a) M. L. Foo, R. Matsuda, Y. Hijikata, R. Krishna, H. Sato, S. Horike, A. Hori, J. Duan, Y. Sato, Y. Kubota, M. Takata, S. Kitagawa, *J. Am. Chem. Soc.* **2016**, *138*, 3022 – 3030; b) J. Lee, C. Y. Chuah, J. Kim, Y. Kim, N. Ko, Y. Seo, K. Kim, T. H. Bae, E. Lee, *Angew. Chem. Int. Ed.* **2018**, *57*, 7869 – 7873; *Angew. Chem.* **2018**, *130*, 7995 – 7999; c) H. Li, C. Liu, C. Chen, Z. Di, D. Yuan,

J. Pang, W. Wei, M. Wu, M. Hong, *Angew. Chem. Int. Ed.* **2021**, *60*, 7547 – 7552; *Angew. Chem.* **2021**, *133*, 7625 – 7630.

[2] a) K. J. Chen, H. S. Scott, D. G. Madden, T. Pham, A. Kumar, A. Bajpai, M. Lusi, K. A. Forrest, B. Space, J. J. Perry IV, M. J. Zaworotko, *Chem* **2016**, *1*, 753 – 765; b) F. Luo, C. Yan, L. Dang, R. Krishna, W. Zhou, H. Wu, X. L. Dong, Y. Han, T.-L. Hu, M. O'Keeffe, L. Wang, M. Luo, R.-B. Lin, B. Chen, *J. Am. Chem. Soc.* **2016**, *138*, 5678 – 5684.

[3] a) S. Liu, X. Han, Y. Chai, G. Wu, W. Li, J. Li, I. da Silva, P. Manuel, Y. Cheng, L. L. Daemen, A. J. Ramirez-Cuesta, W. Shi, N. Guan, S. Yang, L. Li, *Angew. Chem. Int. Ed.* **2021**, *60*, 6526 – 6532; *Angew. Chem.* **2021**, *133*, 6600 – 6606; b) C. T. He, Z. M. Ye, Y. T. Xu, D. D. Zhou, H. L. Zhou, D. Chen, J. P. Zhang, X. M. Chen, *Chem. Sci.* **2017**, *8*, 7560 – 7565; c) Y. Gu, J.-J. Zheng, K. Otake, M. Shivanna, S. Sakaki, H. Yoshino, M. Ohba, S. Kawaguchi, Y. Wang, F. Li, S. Kitagawa, *Angew. Chem. Int. Ed.* **2021**, *60*, 11688 – 11694; *Angew. Chem.* **2021**, *133*, 11794 – 11800; d) J.-P. Zhang, X.-M. Chen, *J. Am. Chem. Soc.* **2009**, *131*, 5516 – 5521.

[4] a) B. R. Barnett, M. I. Gonzalez, J. R. Long, *Trends Chem.* **2019**, *1*, 159 – 171; b) K. Adil, Y. Belmabkhout, R. S. Pillai, A. Cadiau, P. M. Bhatt, A. H. Assen, G. Maurin, M. Eddaoudi, *Chem. Soc. Rev.* **2017**, *46*, 3402 – 3430; c) X. Zhao, Y. Wang, D. S. Li, X. Bu, P. Feng, *Adv. Mater.* **2018**, *30*, 1705189; d) M. Ding, R. W. Flaig, H.-L. Jiang, O. M. Yaghi, *Chem. Soc. Rev.* **2019**, *48*, 2783 – 2828; e) R.-B. Lin, S. Xiang, W. Zhou, B. Chen, *Chem* **2020**, *6*, 337 – 363.

[5] a) H. Wang, J. Li, *Acc. Chem. Res.* **2019**, *52*, 1968 – 1978; b) L. Yang, X. Cui, Z. Zhang, Q. Yang, Z. Bao, Q. Ren, H. Xing, *Angew. Chem. Int. Ed.* **2018**, *57*, 13145 – 13149; *Angew. Chem.* **2018**, *130*, 13329 – 13333; c) P.-Q. Liao, N.-Y. Huang, W.-X. Zhang, J.-P. Zhang, X.-M. Chen, *Science* **2017**, *356*, 1193 – 1196; d) B. Li, M. Chrzanowski, Y. Zhang, S. Ma, *Coord. Chem. Rev.* **2016**, *307*, 106 – 129; e) H. Li, K. Wang, Y. Sun, C. T. Lollar, J. Li, H.-C. Zhou, *Mater. Today* **2018**, *21*, 108 – 121; f) Z. Zhang, S. B. Peh, R. Krishna, C. Kang, K. Chai, Y. Wang, D. Shi, D. Zhao, *Angew. Chem. Int. Ed.* **2021**, *60*, 17198 – 17204; *Angew. Chem.* **2021**, *133*, 17335 – 17341.

[6] a) R.-B. Lin, L. Li, H. Wu, H. Arman, B. Li, R.-G. Lin, W. Zhou, B. Chen, *J. Am. Chem. Soc.* **2017**, *139*, 8022 – 8028; b) L. Yang, L. Yan, Y. Wang, Z. Liu, J. He, Q. Fu, D. Liu, X. Gu, P. Dai, L. Li, X. Zhao, *Angew. Chem. Int. Ed.* **2021**, *60*, 4570 – 4574; *Angew. Chem.* **2021**, *133*, 4620 – 4624; c) Z. Niu, X. Cui, T. Pham, G. Verma, P. C. Lan, C. Shan, H. Xing, K. A. Forrest, S. Suepaul, B. Space, A. Nafady, A. M. Al-Enizi, S. Ma, *Angew. Chem. Int. Ed.* **2021**, *60*, 5283 – 5288; *Angew. Chem.* **2021**, *133*, 5343 – 5348; d) L. Zhang, K. Jiang, L. Yang, L. Li, E. Hu, L. Yang, K. Shao, H. Xing, Y. Cui, Y. Yang, B. Li, B. Chen, G. Qian, *Angew. Chem. Int. Ed.* **2021**, *60*, 15995 – 16002; *Angew. Chem.* **2021**, *133*, 16131 – 16138; e) H. Zeng, M. Xie, Y.-L. Huang, Y. Zhao, X.-J. Xie, J.-P. Bai, M.-Y. Wan, R. Krishna, W. Lu, D. Li, *Angew. Chem. Int. Ed.* **2019**, *58*, 8515 – 8519; *Angew. Chem.* **2019**, *131*, 8603 – 8607; f) L. Jiang, N. Wu, Q. Li, J. Li, D. Wu, Y. Li, *Inorg. Chem.* **2019**, *58*, 4080 – 4084.

[7] S. Mukherjee, Y. He, D. Franz, S.-Q. Wang, W.-R. Xian, A. A. Bezrukov, B. Space, Z. Xu, H. He, M. J. Zaworotko, *Chem. Eur. J.* **2020**, *26*, 4923 – 4929.

[8] a) Y. Zhang, J. Hu, R. Krishna, L. Wang, L. Yang, X. Cui, S. Duttwyler, H. Xing, *Angew. Chem. Int. Ed.* **2020**, *59*, 17664 – 17669; *Angew. Chem.* **2020**, *132*, 17817 – 17822; b) Y. Zhang, L. Wang, J. Hu, S. Duttwyler, X. Cui, H. Xing, *CrystEngComm* **2020**, *22*, 2649 – 2655; c) Y. Zhang, L. Yang, L. Wang, S. Duttwyler, H. Xing, *Angew. Chem. Int. Ed.* **2019**, *58*, 8145 – 8150; *Angew. Chem.* **2019**, *131*, 8229 – 8234; d) Y. Zhang, L. Yang, L. Wang, H. Xing, *J. Mater. Chem. A* **2019**, *7*, 27560 – 27566; e) L. Wang, W. Sun, S. Duttwyler, Y. Zhang, *J. Solid State Chem.* **2021**, *299*, 122167.

[9] a) H.-L. Jiang, T. A. Makal, H.-C. Zhou, *Coord. Chem. Rev.* **2013**, *257*, 2232 – 2249; b) T. T. M. Nguyen, H. M. Le, Y. Kawazoe, H. L. Nguyen, *Mater. Chem. Front.* **2018**, *2*, 2063 – 2069.

[10] Y.-L. Peng, T. Pham, P. Li, T. Wang, Y. Chen, K.-J. Chen, K. A. Forrest, B. Space, P. Cheng, M. J. Zaworotko, Z. Zhang, *Angew. Chem. Int. Ed.* **2018**, *57*, 10971 – 10975; *Angew. Chem.* **2018**, *130*, 11137 – 11141.

[11] Y. Ye, Z. Ma, R.-B. Lin, R. Krishna, W. Zhou, Q. Lin, Z. Zhang, S. Xiang, B. Chen, *J. Am. Chem. Soc.* **2019**, *141*, 4130 – 4136.

[12] J. Pei, K. Shao, J.-X. Wang, H.-M. Wen, Y. Yang, Y. Cui, R. Krishna, B. Li, G. Qian, *Adv. Mater.* **2020**, *32*, 1908275.

[13] O. T. Qazvini, R. Babarao, S. G. Telfer, *Chem. Mater.* **2019**, *31*, 4919 – 4926.

[14] H. S. Scott, M. Shivanna, A. Bajpai, D. G. Madden, K.-J. Chen, T. Pham, K. A. Forrest, A. Hogan, B. Space, J. J. Perry IV, M. J. Zaworokto, *ACS Appl. Mater. Interfaces* **2017**, *9*, 33395 – 33400.

[15] a) R. Krishna, *RSC Adv.* **2017**, *7*, 35724 – 35737; b) R. Krishna, *Sep. Purif. Technol.* **2018**, *194*, 281 – 300; c) R. Krishna, *ACS Omega* **2020**, *5*, 16987 – 17004.

Manuscript received: June 15, 2021
Revised manuscript received: July 20, 2021
Accepted manuscript online: August 12, 2021
Version of record online: September 14, 2021

Angewandte Chemie
Eine Zeitschrift der Gesellschaft Deutscher Chemiker

Supporting Information

Interpenetration Symmetry Control Within Ultramicroporous Robust Boron Cluster Hybrid MOFs for Benchmark Purification of Acetylene from Carbon Dioxide

Lingyao Wang[+], Wanqi Sun[+], Yuanbin Zhang, Nuo Xu, Rajamani Krishna, Jianbo Hu, Yunjia Jiang, Yabing He, and Huabin Xing**

anie_202107963_sm_miscellaneous_information.pdf

I General Information and Procedures

Unless otherwise noted, all the reactions were performed under air without N_2 or Ar protection. All reagents were used as received without purification unless stated otherwise.

Chemicals: The basic starting material $[Na]_2[B_{12}H_{12}]$ was purchased from Yuanli Technology Company without further purification. 1,2-Di(4-pyridyl)ethylene was purchased from Energy Chemical and Meryer without further purification. The purity of all the organic compounds was identified by ^1H NMR and $^{13}C\{^1H\}$ NMR. $Cu[NO_3]_2{\cdot}3H_2O$ was purchased from Macklin without further purification. All other reagents were purchased from Adamas-beta and used without further purification.

Preparation of single crystals of ZNU-1 (also termed as BSF-9 in sequence): To a 4 mL long thin tube was added a 1 mL of aqueous solution with $[Na]_2[B_{12}H_{12}]$ (~ 2 mg) and $Cu[NO_3]_2{\cdot}3H_2O$ (~ 2 mg). 1 mL of MeOH/H_2O mixture was slowly layered above the solution, followed by a 1 mL of MeOH solution of 1,2-di(4-pyridyl)ethylene (4 mg). The tube was sealed and left undisturbed at 298 K. After ~1 week, violet single crystals suitable for X-ray diffraction analysis were obtained.

Bulky synthesis of ZNU-1 (also termed as BSF-9 in sequence): A mixture of $[Na]_2[B_{12}H_{12}]$ (225 mg, 1.2 mmol, 1.2 equiv) and $Cu[NO_3]_2{\cdot}3H_2O$ (242 mg, 1 mmol, 1 equiv) was dissolved in 10 mL of water in a 100 mL round bottom flask and heated to 35 °C. Then a MeOH (30 mL) solution of 1,2-di(4-pyridyl)ethylene (dpe) (364 mg, 2 mmol, 2 equiv) was slowly added to the above solution during string (500 rpm). Gray violet solid formed immidiately, and the suspension was stirred at 35 °C for another 48 h. The solid was then collected by filtration, washed by MeOH (10 mL), and soaked in anhydrous MeOH for storage.

Ligands / Anions	1,2-bis(4-pyridyl) acetylene **bpa**	1,4-di(pyridin-4-yl)benzene **dpb**	4,4'-azopyridine **apy**	4,4'-dipyridine **dpy**	1,2-di(4-pyridyl) ethylene **dpe**
$[B_{12}H_{12}]^{2-}$	BSF-1 $CuB_{12}H_{12}(bpa)_2$ BSF-6 $CuB_{12}H_{12}(bpa)_2$	BSF-3 $CuB_{12}H_{12}(dpb)_2$ BSF-3-Co $CoB_{12}H_{12}(dpb)_2$ BSF-7 $CuB_{12}H_{12}(dpb)_2$	BSF-4 $CuB_{12}H_{12}(apy)_2$ BSF-5 $CuB_{12}H_{12}(apy)_2$	BSF-8 $CuB_{12}H_{12}(dpy)_2$	ZNU-1 (BSF-9) $CuB_{12}H_{12}(dpe)_2$ **(This work)**
$[B_{12}H_{11}I]^{2-}$	BSF-2 $CuB_{12}H_{11}I(bpa)_2$	BSF-61 $CuB_{12}H_{11}I(dpb)_2$	BSF-21 $CuB_{12}H_{11}I(apy)_2$		
$[B_{12}Cl_{12}]^{2-}$		BSF-71, 72, 73, 74, 75			
Note: Blue color means the framework is interpenetrated, namely, BSF-1, BSF-2, BSF-21, BSF-3, BSF-3-Co, BSF-4 and ZNU-1 (BSF-9) are interpenetrated; green color means the the framework is non-interpenetrated, namely, BSF-6, BSF-61, BSF-7, and BSF-8 are non-interpenetrated; brown color means the framework has metal ions coordinated to solvents, namely, BSF-71, BSF-72, BSF-73, BSF-74, BSF-75 have metal ions coordinated to solvents					

Single-crystal X-ray diffraction studies were conducted at 193 K on a BrukerAXS D8 VENTURE diffractometer equipped with a PHOTON-100/CMOS detector (GaKα, λ = 1.34139 Å). Indexing was performed using APEX2. Data integration and reduction were completed using SaintPlus 6.01. Absorption correction was performed by the multi-scan method implemented in SADABS. The space group was determined using XPREP implemented in APEX2.1 The structure was solved with SHELXS-97 (direct methods) and refined on F2 (nonlinear least-squares method) with SHELXL-97 contained in APEX2, WinGX v1.70.01, and OLEX2 v1.1.5 program packages. All non-hydrogen atoms were refined anisotropically. The contribution of disordered solvent molecules was treated as diffuse using the Squeeze routine implemented in Platon.

Powder X-ray diffraction (PXRD) data were collected on a Bruker AXS D8-Advance diffractometer (Cu Kαλ = 1.540598 Å) with an operating power of 40 KV, 30 mA and a scan speed of 4.0°/min. The range of 2θ was from 5° to 50°.

Thermal gravimetric analysis was performed on a TGA Q500 V20.13 Build 39 instrument. Experiments were carried out using a platinum pan under nitrogen atmosphere which conducted by a flow rate of 60 mL/min nitrogen gas. First, the sample was heated at 80 °C for 1 h to remove the water residue and equilibrated for 5 minutes, then cooled down to 50 °C. The data were collected at the temperature range of 50 °C to 800 °C with a ramp of 10 °C /min.

The gas adsorption measurements were performed on an Autosorb iQ instrument. Before gas adsorption measurements, the sample of ZNU-1 (single crystals) was evacuated at 75 ºC for 1 day until the pressure dropped below 7 μmHg. The sorption isotherms were collected at 288, 298, and 308 K on activated samples.

Fitting of experimental data on pure component isotherms

The unary isotherms for C_2H_2 and CO_2, measured at three different temperatures 288 K, 298 K, and 308 K in ZNU-1 were fitted with excellent accuracy using the dual-site Langmuir model, where we distinguish two distinct adsorption sites A and B:

$$q = \frac{q_{sat,A} b_A p}{1 + b_A p} + \frac{q_{sat,B} b_B p}{1 + b_B p} \tag{S1}$$

Here, P is the pressure of the bulk gas at equilibrium with the adsorbed phase (Pa), q is the adsorbed amount per mass of adsorbent (mol kg^{-1}), $q_{sat,\,A}$ an $q_{sat,\,B}$ are the saturation capacities of site A and B (mol kg^{-1}), b_A and b_B are the affinity coefficients of site A and B (Pa^{-1}).

In eq (S1), the Langmuir parameters b_A, b_B are both temperature dependent

$$b_A = b_{A0} \exp\left(\frac{E_A}{RT}\right); \quad b_b = b_{B0} \exp\left(\frac{E_B}{RT}\right) \tag{S2}$$

In eq (S2), E_A, E_B are the energy parameters associated with sites A, and B, respectively.

The isosteric heat of adsorption, Q_{st}, is defined as

$$Q_{st} = -RT^2 \left(\frac{\partial \ln p}{\partial T} \right)_q \tag{S3}$$

where the derivative in the right member of eq (S3) is determined at constant adsorbate loading, q. The calculations are based on the use of the Clausius-Clapeyron equation.

IAST calculations of adsorption selectivity and uptake capacities:

For screening MOFs for separation of binary mixtures of components 1 and 2, the adsorption selectivity, S_{ads}, is defined by

$$S_{ads} = \frac{q_1 / q_2}{y_{10} / y_{20}} \tag{S4}$$

In eq (S4), y_{10}, y_{20} are the mole fractions of the bulk gas phase mixture.

The C_2H_2(1)/CO_2(2) mixture separations are envisaged to be carried out in fixed bed adsorbers. In such devices, the separations are dictated by a combination of adsorption selectivity and uptake capacity. Using the shock wave model for fixed bed adsorbers, Krishna[1, 2] has suggested that the appropriate metric is the separation potential, Δq_1. The appropriate expression describing the productivity of pure C_2H_2 in the desorption phase of fixed-bed operations is

$$\Delta q_1 = q_1 - q_2 \frac{y_{10}}{y_{20}} \tag{S5}$$

In eq (S5) y_{10}, y_{20} are the mole fractions of the feed mixture during the adsorption cycle. In the derivation of eq (S5), it is assumed that the concentration "fronts" traversed the column in the form of shock waves during the desorption cycle. The molar loadings q_1, q_2 of the two components are determined using the Ideal Adsorbed Solution Theory (IAST) of Myers and Prausnitz using the unary isotherm fits as data inputs.[3] The physical significance of Δq_1 is the maximum productivity of pure C_2H_2(1) that is achievable in PSA operations.

Transient breakthrough simulations

With both MOFs, C_2H_2 is selectively adsorbed. The desired C_2H_2 product is available in the blowdown phase of the Skarstrom cycle of fixed bed operations, as shown in the schematic in Figure S1.

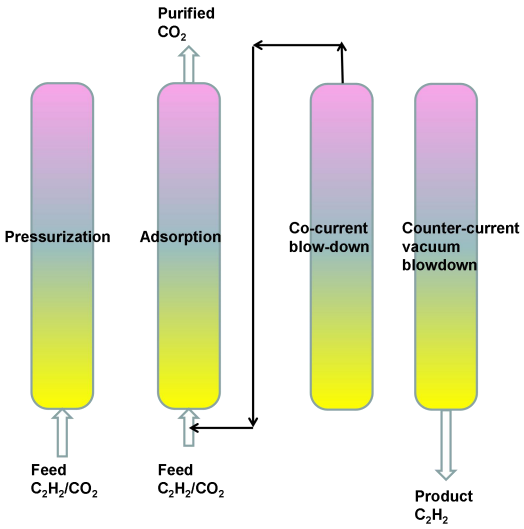

Figure S1. Sequential steps in the operation of a fixed-bed adsorber in the Skarstrom cycle for $C_2H_2(1)/CO_2(2)$ separation. This scheme is reproduced from Figure 7 of Krishna.[2]

Transient breakthrough simulations of the adsorption/desorption cycles were carried out for binary 50/50 C_2H_2/CO_2 mixtures in ZNU-1 and BSF-4 operating at a total pressure of 100 kPa and 298 K, using the methodology described in earlier publications.[1, 2, 4-6] In these simulations, intra-crystalline diffusion influences are ignored.

For comparing the separation performance of MOFs, we carried out simulations of transient desorption in which we choose: cross-sectional area, A = 1 m^2; superficial gas velocity at the entrance to the bed, $u_0 = 0.04$ m s^{-1}; voidage of the packed bed, ε = 0.4. We choose the mass of the adsorbent in the bed $m_{ads} = 180$ kg, cross-sectional area, A = 1 m^2; superficial gas velocity at the bed inlet, u_0 = 0.04 m s^{-1};

voidage of the packed bed, ε = 0.4. The interstitial gas velocity $v = \frac{u}{\varepsilon}$. If the total length of the bed is L m, the total volume of the bed is $V_{bed} = LA$. The volume of zeolite or MOF used in the simulations is $V_{ads} = LA(1-\varepsilon)$. It is important to note that the volume of adsorbent, V_{ads}, includes the pore volume of the adsorbent material. If ρ is the framework density, the mass of the adsorbent in the bed is $m_{ads} = (1-\varepsilon)\times(L \text{ m})\times(A \text{ m}^2)\times(\rho \text{ kg m}^{-3})$ kg.

For presenting the breakthrough simulation results, we may use the dimensionless time, $\tau = \frac{tu}{L\varepsilon}$, obtained by dividing the actual time, t, by the characteristic time, $\frac{L}{v} = \frac{\varepsilon L}{u_0}$, where L is the length of adsorber, v is the interstitial gas velocity.

For comparison of breakthrough simulations with breakthrough experiments, it is most convenient to use $\frac{Q_0 t}{m_{ads}}$ as the x-axis when presenting the breakthrough simulation data

$$\frac{(Q_0 = \text{flow rate mL min}^{-1} \text{ at STP})\times(\text{time in min})}{(\text{g MOF packed in tube})} = \frac{Q_0 t}{m_{ads}} = \text{mL g}^{-1} \qquad \text{(S6)}$$

Simulations of the counter-current blowdown phase are shown in Figure S20b,c.

In practice, counter-current blowdown will be initiated just before C_2H_2(1) breaks through in the adsorption cycle. In our simulations, the adsorption phase was terminated at $t = 700$ s; τ=233.3 for ZNU-1. For BSF-4, the adsorption phase was terminated at $t = 442$ s; τ=147.3. The start of the blowdown phase is indicated by the arrows in Figure S20a.

In our simulations, deep vacuum (= 2 Pa) was applied. Since the characteristics of the vacuum pump are not known, it is arbitrarily assumed that the interstitial velocity

in the fixed bed is maintained at $v = \frac{u}{\varepsilon} = 0.1$ m s^{-1}. Desorption is a much slower process, and the time required for total recovery of adsorbed components is large.

Figure S20b plots the cumulative moles of C_2H_2(1) and CO_2(2) recovered during blowdown using deep vacuum. The recovered amounts of C_2H_2 during blowdown agrees very closely with the values of $\Delta q_1 = q_1 - q_2 \frac{y_{10}}{y_{20}}$, that are determined from IAST. The productivity C_2H_2 is significantly higher with ZNU-1, as compared to BSF-4.

Since CO_2(2) also desorbs during blowdown operations, it is not possible to obtain 100% pure C_2H_2. The purities of recovered C_2H_2 during blowdown are plotted in Figure S20c. With ZNU-1, 98% purity is achievable, whereas with BSF-4, the maximum purity of C_2H_2(1) is only 90%.

Breakthrough experiments

The breakthrough experiments were carried out in the dynamic gas breakthrough equipment HP-MC41. The experiments were conducted using a stainless steel column (5 mm inner diameter × 200 mm length or 4.9 mm inner diameter × 100 mm length). The weight of and ZNU-1 packed in the columns were 2.14 g and 1.03 g, respectively. The column packed with sample was first purged with a Ar flow (5 mL min^{-1}) for 24 h at 75 °C. The mixed gas of C_2H_2/CO_2 (50/50, v/v/) was then introduced. Outlet gas from the column was monitored using gas chromatography (GC-9860-5CNJ) with the thermal conductivity detector TCD. After the breakthrough experiment, the sample was regenerated with a Ar flow of 5 mL min^{-1} under 75 °C for 8 h.

The illustration of the gas breakthrough equipment working mechanism is showing as below: A) under work; B) under purge; C) under vacuum.

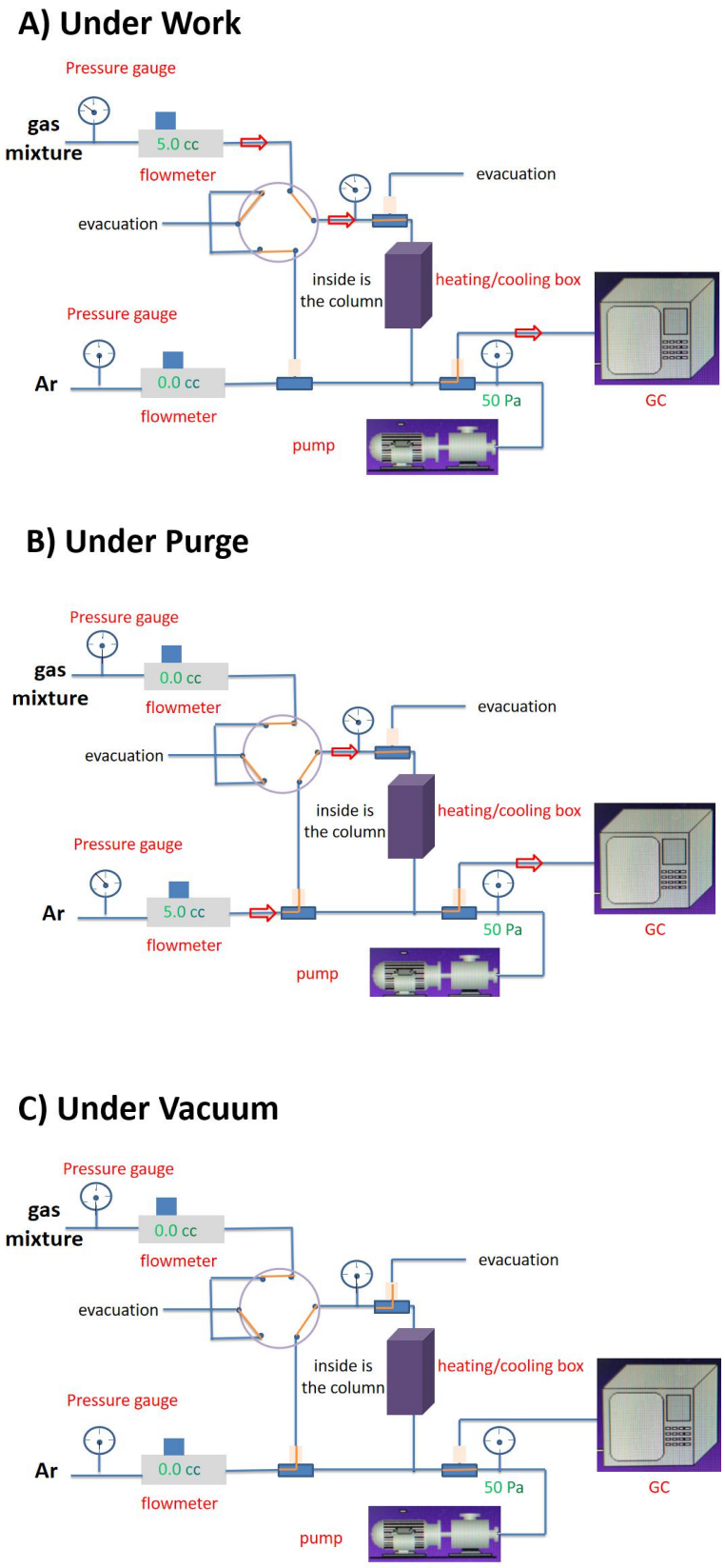

Figure S2. The illustration of the gas breakthrough equipment working mechanism containing gas pipelines, pressure gauge, flowmeter, GC and pump: A) under work; B) under purge; C) under vacuum.

Calculation of separation factor (α)

The amount of gas adsorbed i (q_i) is calculated from the breakthrough curve using the following:

$$q_i = \frac{V_T P_i \Delta T}{m}$$

Here, V_T is the total flow rate of gas (cm^3/min), P_i is the partial pressure of gas i (atm), ΔT is the time for initial breakthrough of gas i to occur (mins) and m is the mass of the sorbent (g). The separation factor (α) of the breakthrough experiment is determined as

$$\alpha = \frac{q_1 y_2}{q_2 y_1}$$

Where, y_i is the partial pressure of gas i in the gas mixture.

Grand canonical Monte Carlo (GCMC) simulations

GCMC simulaitons were performed in MS 2017R2 package using sorption module. The structure of ZNU-1 was firstly optimized *via* DFT geometry optimization. The Mulliken charges for atoms of ZNU-1 were derived from DFT calculation. The simulations adopted the locate task, Metropolis method in sorption module and the universal force field (UFF). The Qeq charges for atoms of ZNU-1 were selected in GCMC simulations. During the simulation, the framework was considered to be rigid during the simulation and the interaction energy between the adsorbed molecules and the framewrok were computed through the Coulomb and Lennard-Jones 6-12 (LJ) potentials. The cutoff radius was chosen 18.5 Å for Van der Walls interaction and the long range electrostatic interactions were handled using the Ewald summation method. The loading steps and the equilibration steps were 1×10^7, the production steps were 1×10^7. The C_2H_2 model were taken from Yuan et al. (Nat. Commun. 2015, 6, 7515). The cutoff radius was chosen 18.5 Å for Van der Walls interaction and the long range electrostatic interactions were handled using the Ewald summation method. The loading steps and the equilibration steps were 1×10^7, the production steps were 1×10^7.

Density functional theory (DFT) calculations

The DFT calculation were performed using the Gaussian package. The PBE0 functionals with the Grimme's D3(BJ) dispersion correction were applied to DFT calculations along with the 6-311+G(d,p) basis set. All structures were optimized without any symmetry constraints and the optimized minimum-energy structures were verified as stationary points on the potential energy surface by performing numerical harmonic vibrational frequency calculations. The equation for the calculation of binding energy (ΔE) is defined as: $\Delta E = E(MOF+gas) - [E(MOF) + E(gas)]$.

To gain insight into the interpenetration difference between BSF-4 and ZNU-1, we calculated the potential energy curves for both structures by shifting one net to change the interpenetration mode with Castep package using a GGA/PBE level of theory and DNP basis set. We first constructed several configures with one net moving along a axis direction for 0~3 Å. Under this circumstance, the asymmetrically interpenetrated BSF-4 became nearly symmetrically interpenetrated while symmetrically interpenetrated ZNU-1 became asymmetrically interpenetrated. The single energy calculation was performed for every configuration, and the framework potential energies curves were described.

Reference:

(1) Krishna, R. Screening Metal-Organic Frameworks for Mixture Separations in Fixed-Bed Adsorbers using a Combined Selectivity/Capacity Metric. *RSC Adv.* **2017**, *7*, 35724-35737.

(2) Krishna, R. Metrics for Evaluation and Screening of Metal-Organic Frameworks for Applications in Mixture Separations. *ACS Omega* **2020**, *5*, 16987−17004.

(3) Myers, A. L.; Prausnitz, J. M. Thermodynamics of Mixed Gas Adsorption. *A.I.Ch.E.J.* **1965**, *11*, 121-130.

(4) Krishna, R. The Maxwell-Stefan Description of Mixture Diffusion in Nanoporous Crystalline Materials. *Microporous Mesoporous Mater.* **2014**, *185*, 30-50.

(5) Krishna, R. Methodologies for Evaluation of Metal-Organic Frameworks in Separation Applications. *RSC Adv.* **2015**, *5*, 52269-52295.

(6) Krishna, R. Methodologies for Screening and Selection of Crystalline Microporous Materials in Mixture Separations. *Sep. Purif. Technol.* **2018**, *194*, 281-300.

II Characterization

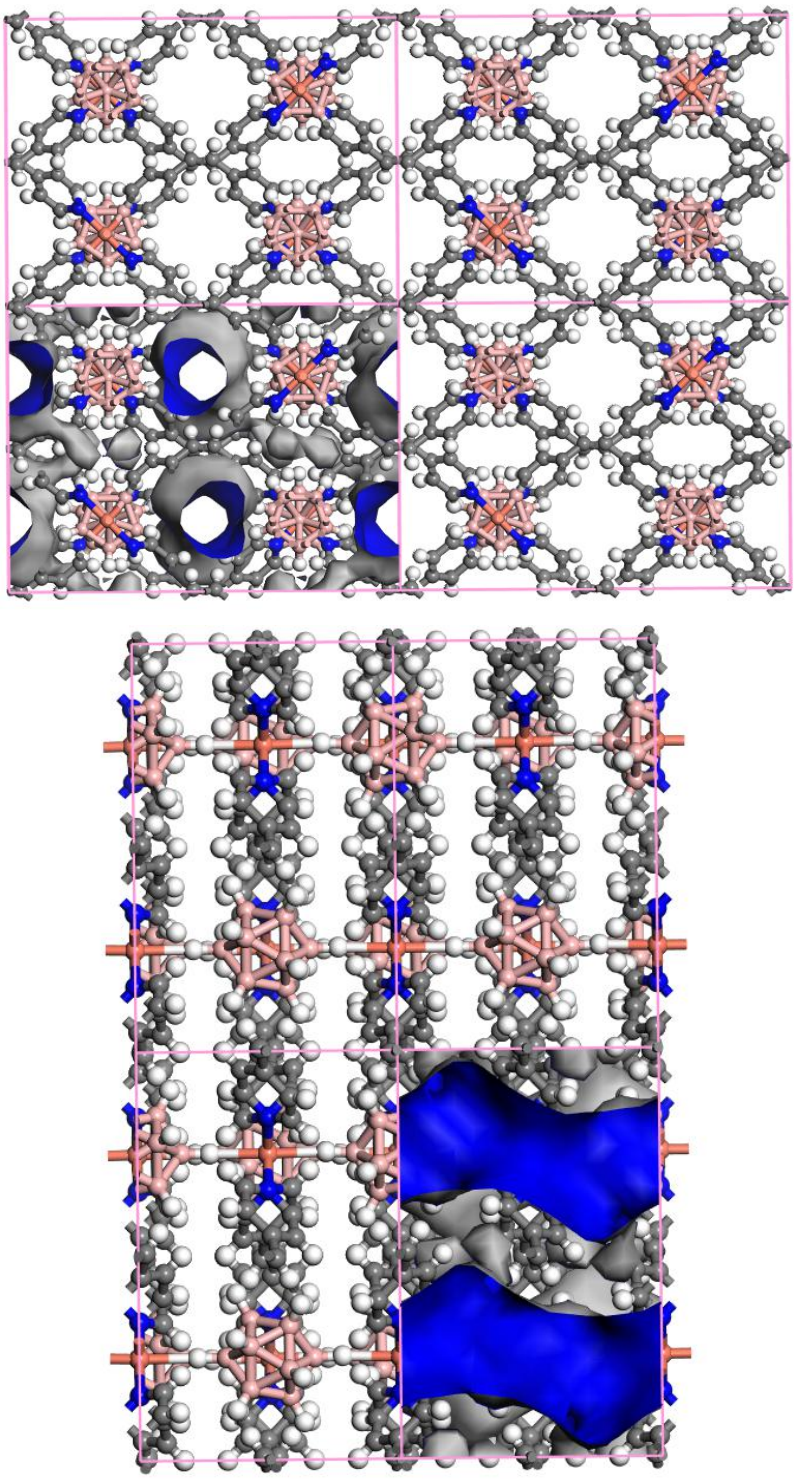

Figure S3. 2 × 2 × 2 packing diagrams of ZNU-1 viewed down the crystallographic *a*-axis (above) and *c*-axis (below) in ball-stick mode with void surface in blue determined using a probe of 1.2 Å by PLATON.

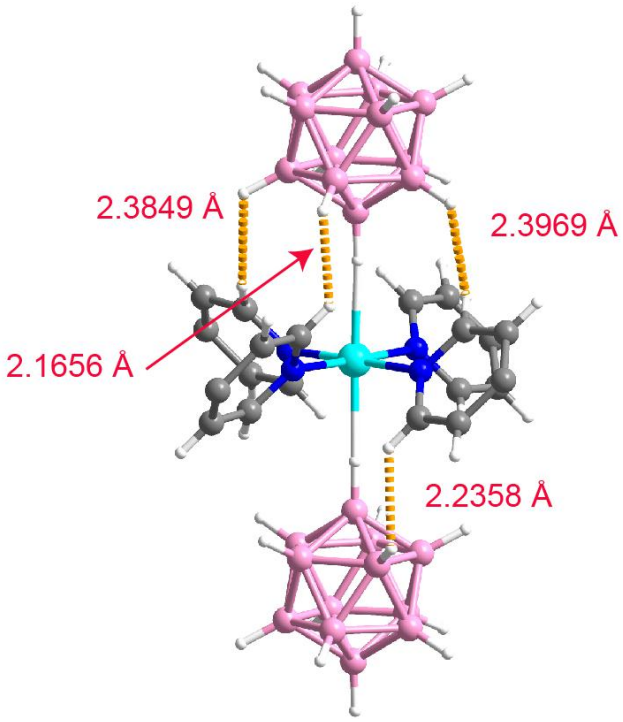

Figure S4. The Cu(II) coordination environment in symmetrically interpenetrated ZNU-1. Multiple B-$H^{\delta-}\cdots H^{\delta+}$-$C_{Py}$ dihydrogen bonds (2.1656-2.3969 Å) between the $[B_{12}H_{12}]^{2-}$ anions and pyridyl groups can be observed. All displayed structures are based on X-ray crystallography. Rose for boron, gray-25% for hydrogen, gray-50% for carbon, blue for nitrogen, turquoise for copper.

Analysis: The packing of two -CH=CH- linkers from different nets is stronger than that of -N=N- linkers. In general, the symmetry mismatch and specific B-$H^{\delta-}\cdots H^{\delta+}$-$C_{Py}$ interactions are two major factors that cause asymmetric interpenetration while close π···π packing of the organic linkers is the major positive factor to promote the symmetric interpenetration. It is difficult to predict which side will dominate the interpenetration modes. Based on the results, only in the structure of ZNU-1, the π···π packing interaction of the linkers overcomes the barrier of symmetry mismatch.

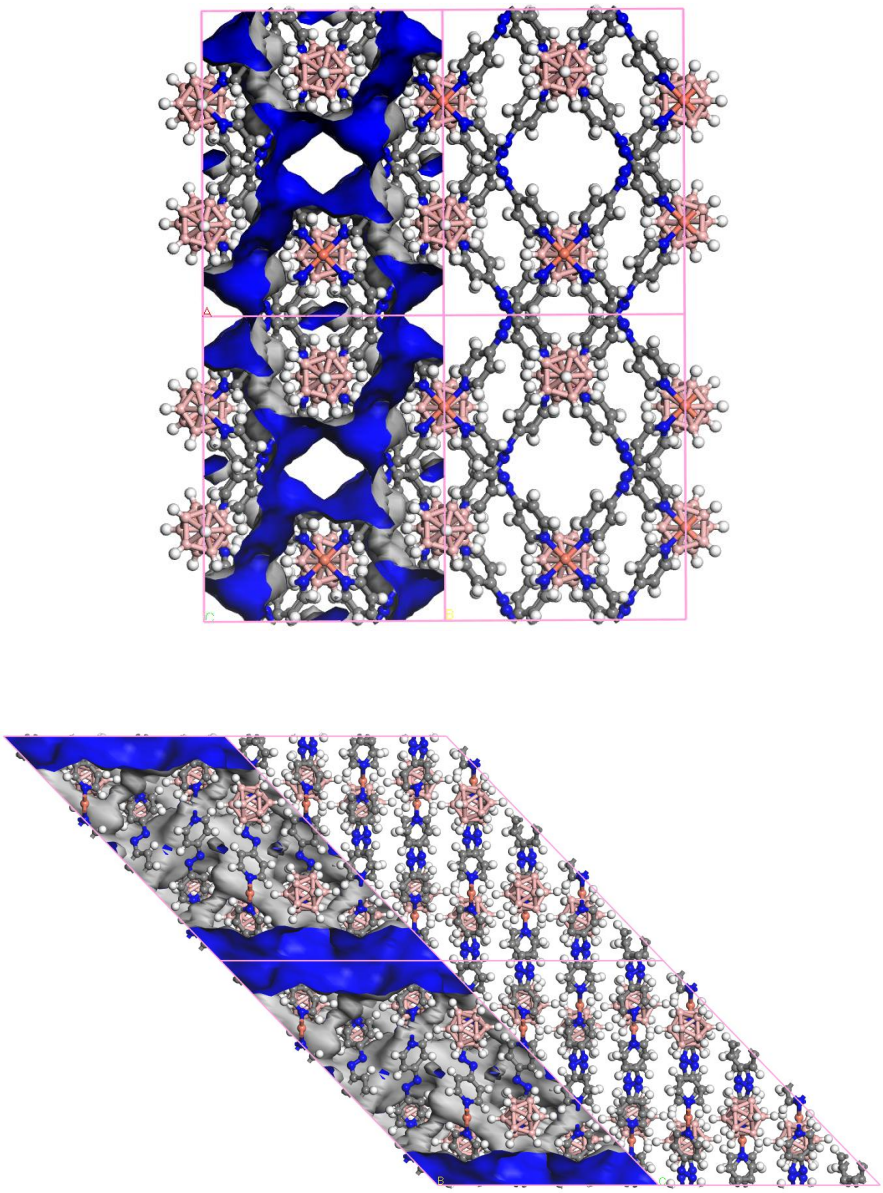

Figure S5. 2 × 2 × 2 packing diagrams of BSF-4 viewed down the crystallographic *c*-axis (above) and *b*-axis (below) in ball-stick mode with void surface in blue determined using a probe of 1.2 Å by PLATON.

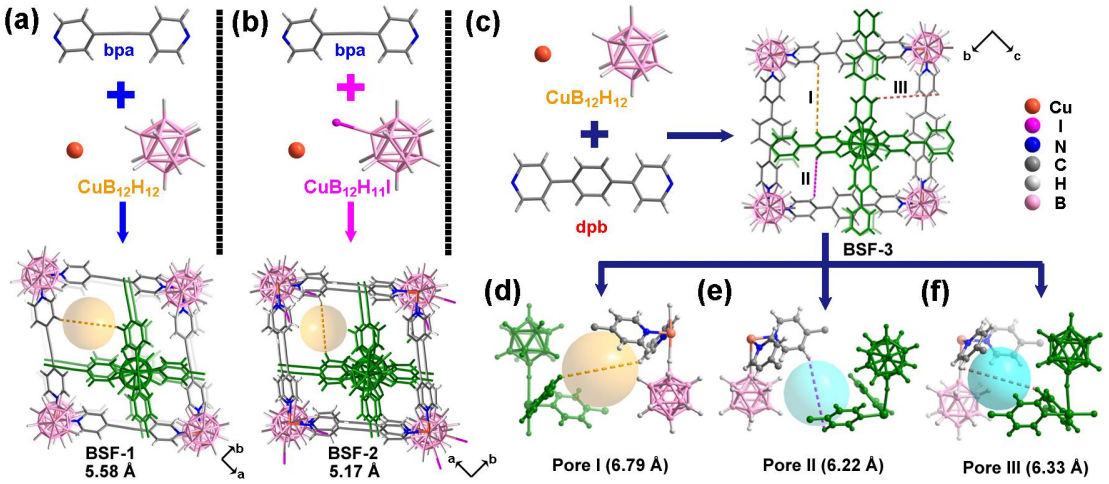

Figure S6. The structure of asymmetrically interpenetrated BSF-1, BSF-2, and BSF-3. All displayed structures are based on X-ray crystallography. Rose for boron, gray-25% for hydrogen, gray-50% for carbon, blue for nitrogen, orange for copper, red for oxygen, purple for iodine.

Analysis： Similar to the structure of BSF-4 (Figure 1C and D), BSF-1, BSF-2, and BSF-3 are all interpenetrated asymmetrically. For BSF-1 and BSF-2 with short linker, only the largest pore is accessible. For BSF-3 with long linker, three pores are accessible. However, the over-sized pore make the synergistic dihydrogen bonding interaction difficult to form.

Table S1 Summary of the crystallographic parameters of BSF-1, BSF-2, BSF-3, BSF-4, and ZNU-1

Materials	BSF-1	BSF-2	BSF-3	BSF-4	ZNU-1
Cell	a=28.764(2)	a=28.398(2)	a=19.8856(17)	a=28.360(3)	a=10.0504(17)
	b=17.1839(11)	b = 17.7840(12)	b=22.4095(18)	b=16.0571(15)	b=15.709(2)
	c=19.918(3)	c = 20.2046(15)	c=21.0263(16)	c=20.1217(19)	c=21.438(3)
	α=90	α= 90	α=90	α=90	α=90
	β=133.107(2)	β= 133.929(2)	β=90	β=134.052(4)	β=90
	γ=90	γ = 90	γ=90	γ=90	γ=90
Temperature	173 K	173 K	193 K	193K	193 K
Volume (Å^3)	7187.6(13)	7348.9(10)	9369.9(13)	6585.5(12)	3384.7(9)
Space group	C 2/c	C 2/c	Ima2	C 2/c	P b c n
Hall group	-C2yc	-C2yc	I2-2a	-C 2yc	-P 2n 2ab
formula	$C_{24}H_{28}B_{12}CuN_4$	$C_{24}H_{27}B_{12}CuIN_4$	$C_{32}H_{36}B_{12}CuN_4$	$C_{20}H_{28}B12CuN_8$	$C_{24}H_{32}B_{12}CuN_4$
MW	565.77	691.65	669.91	573.77	569.81
density	1.046	1.250	0.95	1.157	1.118
Z	8	8	8	8	4
R	0.0684	0.1525	0.0912	0.1116 (15416)	0.0879 (4398)
wR2	0.1859	0.3725	0.2616	0.3138 (24884)	0.3139 (8597)
S	1.043	1.150	1.121	1.078	1.302

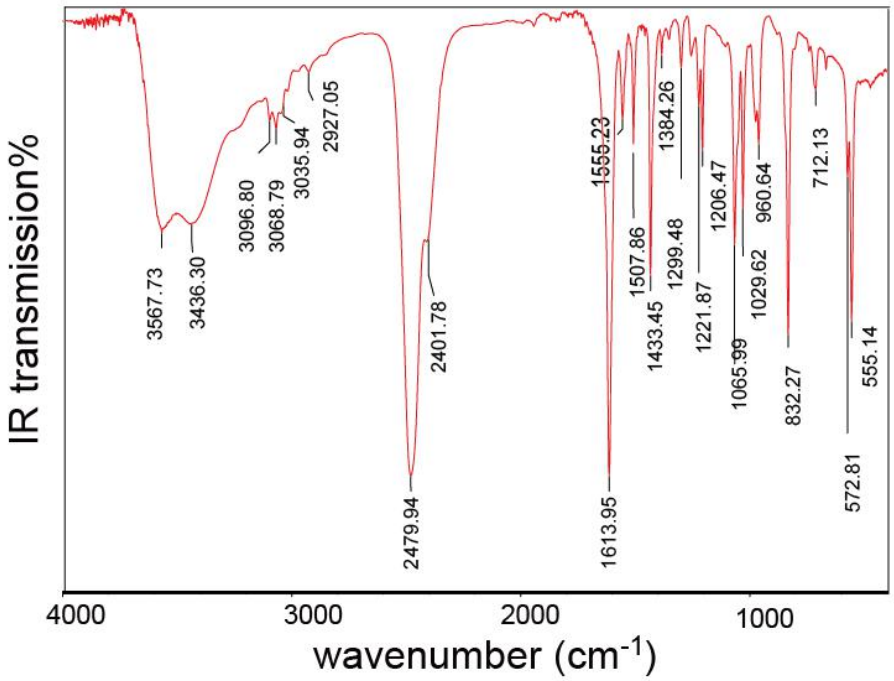

Figure S7. IR spectrum of ZNU-1 after activation.

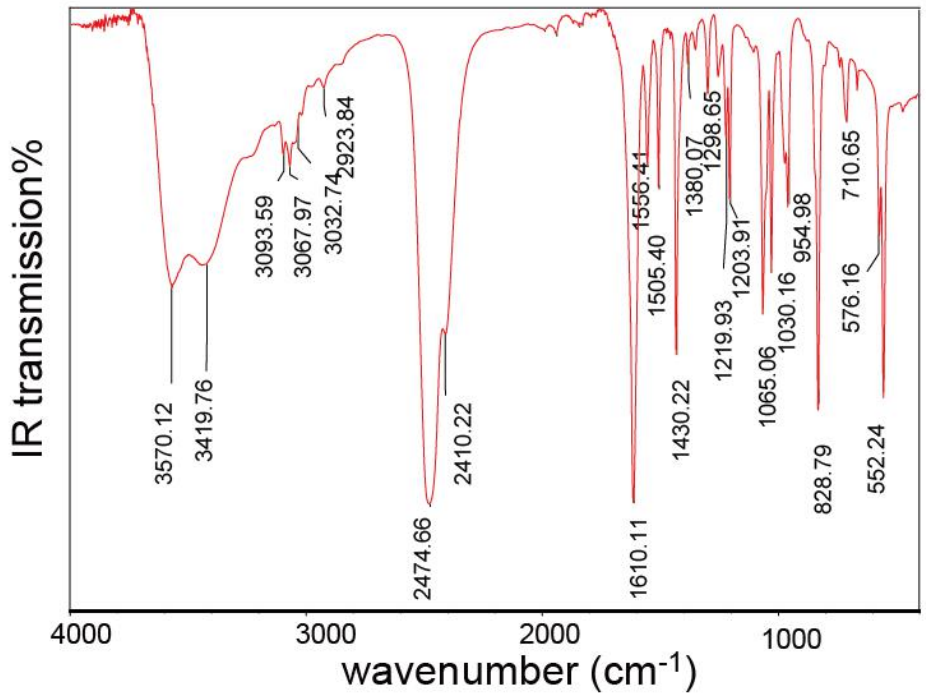

Figure S8. IR spectrum of ZNU-1 after activation followed by exposure to C_2H_2 (1 atm) balloon for 3 hours.

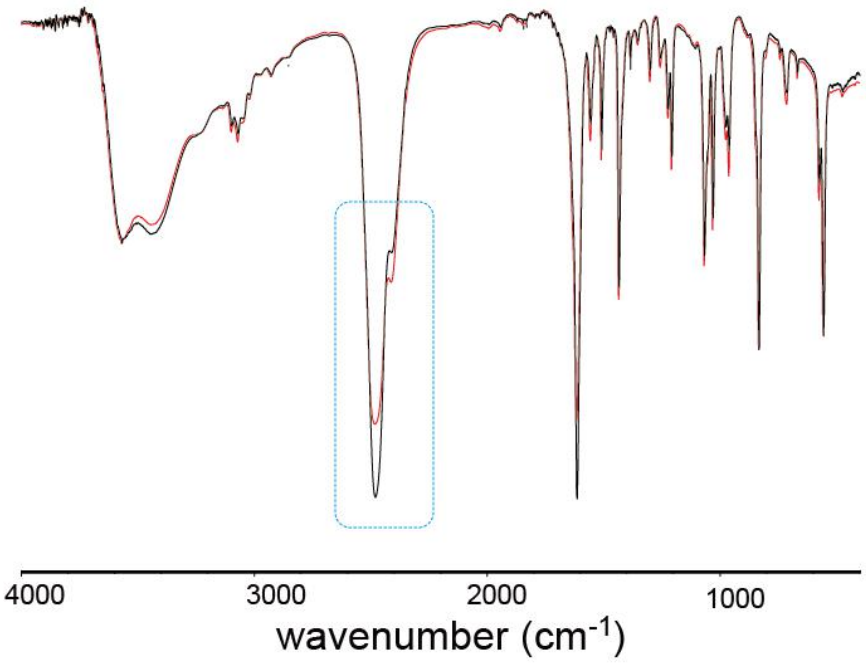

Figure S9. IR spectra stack of ZNU-1 after activation (black curves) and after activation followed by exposure to C_2H_2 (1 atm) balloon for 3 hours (red curves).

Analysis: the broad peak in the region of 2480-2400 cm^{-1} belongs to the B-H stretch. The sharp and large one is for free B-H groups, while the small shoulder peak belongs to the "locked" B-H groups that are coordinating to the Cu(II) ion or interact with the pyridyl group by B-$H^{\delta-}\cdots^{\delta+}$H-C dihydrogen bonding. After exposure to C_2H_2 the activated ZNU-1 can adsorb some C_2H_2 into the pores. While other peaks almost kept the same, a big difference was observed for B-H signals. As B-H moieties can strongly interact with C_2H_2 molecules, the free B-H groups decrease and the "locked" B-H groups increase due to the multiple interactions with C_2H_2 as indicated by DFT-D calculation. This also gave evidence that the electronegative B-H groups were the main bonding sites for C_2H_2. No signals from the C_2H_2 molecules could be observed due to the low concentration.

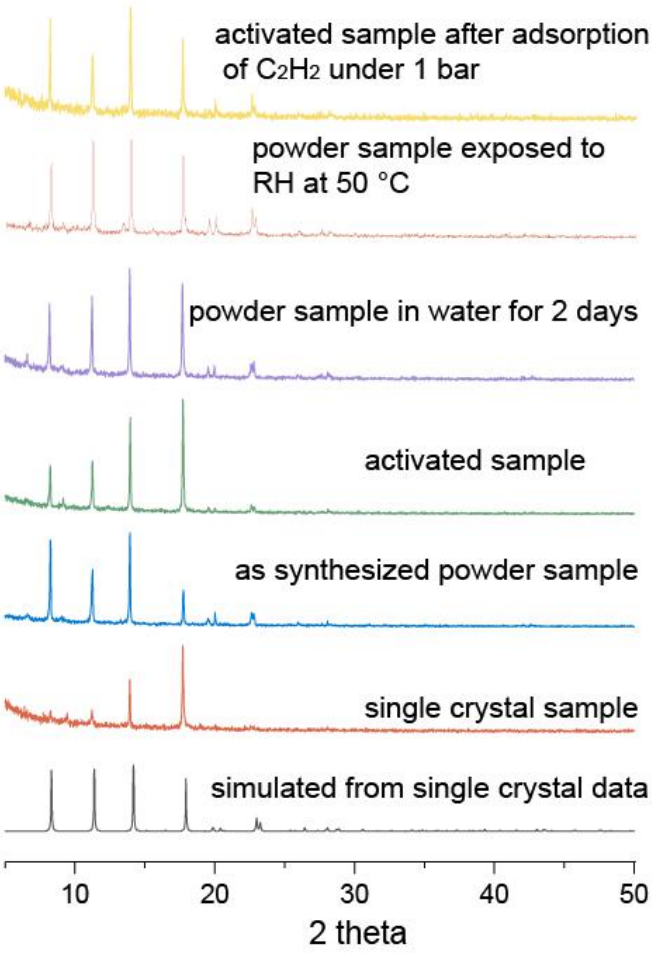

Figure S10. PXRD patterns of ZNU-1 under different conditions and treatment.

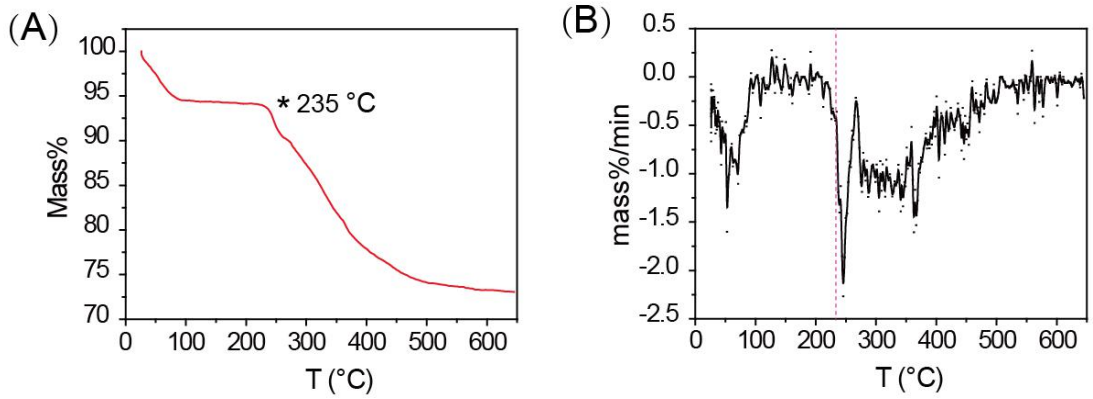

Figure S11. TGA (A) and DTG (B) curves of ZNU-1. The weight loss between 50-100 ºC is because of the loss of MeOH and water from the sample. The weights keep consistent until ~235 ºC.

III Adsorption data, IAST selectivity and *Q*st

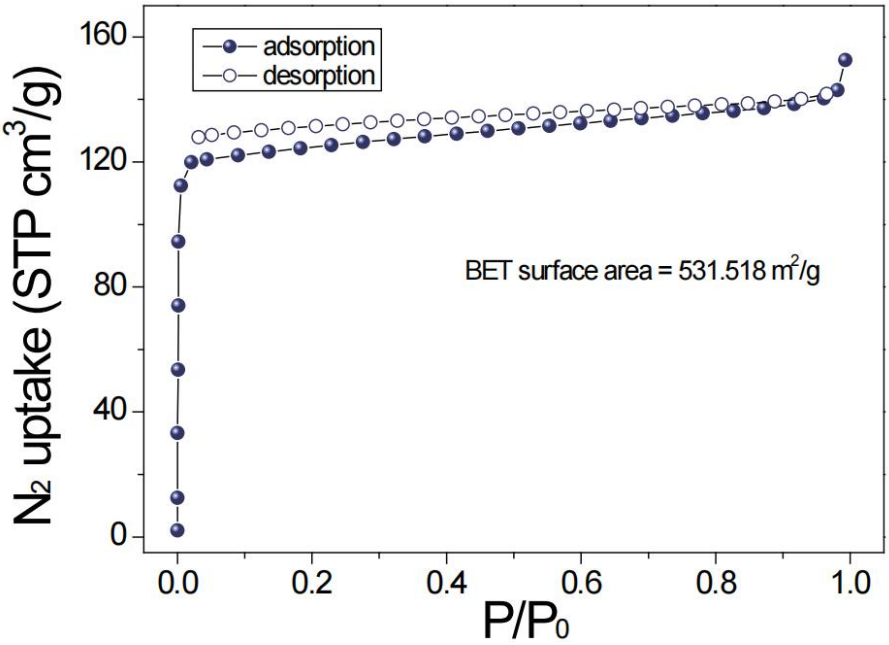

Figure S12. The sorption isotherm of N_2 on ZNU-1 at 77 K.

The BET surface area calculated from the N_2 adsorption isotherms under the pressure range of P/P_0 = 0.0001-0.01 (for ultramicropores) is ~ 531. 518 m^2/g.

MBET summary:

Slope = 6.547 1/g;

Intercept = 5.088×10^{-3} 1/g;

Correlation coefficient, r= 0.999099;

C constant = 1287.866.

Analysis: The experimental BET surface area (~ 531. 518 m^2/g) was very consistent with the theoretical value of 545.198 m^2/g, indicating the activation process is successful.

Table S2. Comparison of C_2H_2 and CO_2

Gas molecules	Dynamic Size (Å)	Molecular size (Å^3)	Boiling point (K)	Quadrupole Moment (C m^2)
C_2H_2	3.3	3.32 x 3.34 x 5.70	189.3	20.5 x 10^{-40}
CO_2	3.3	3.18 x 3.33 x 5.36	194.7	-13.4 x 10^{-40}

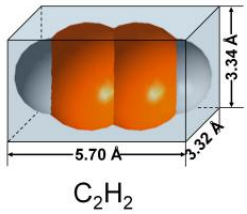

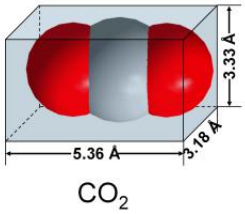

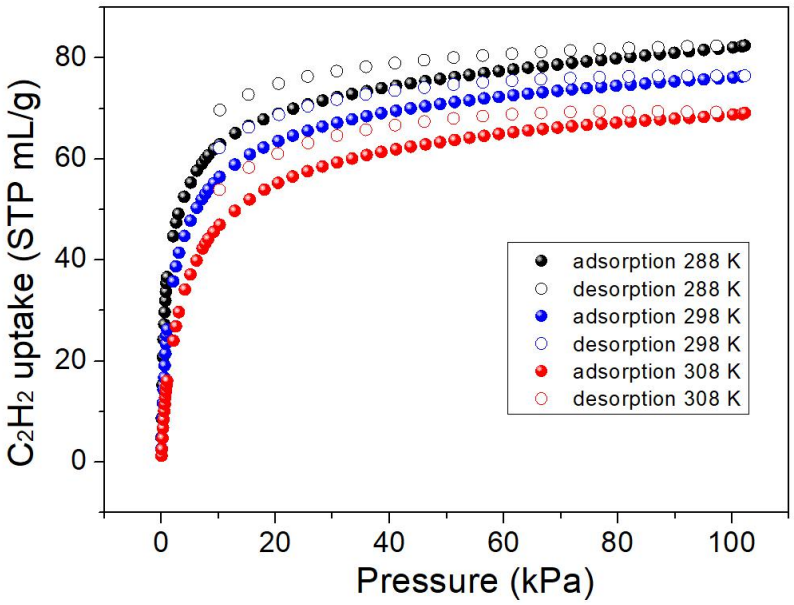

Figure S13. The sorption isotherm of C_2H_2 on ZNU-1 at 288, 298, and 308 K.

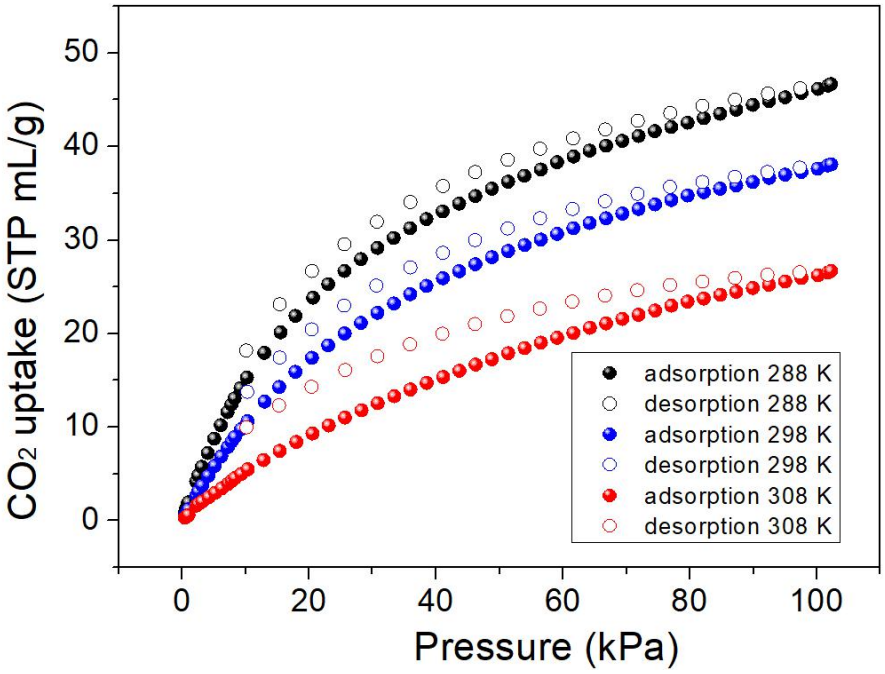

Figure S14. The sorption isotherm of CO_2 on ZNU-1 at 288, 298, and 308 K.

Table S3. Dual-site Langmuir parameter fits for C_2H_2, and CO_2 in ZNU-1.

	Site A			Site B		
	$q_{A,sat}$ mol kg^{-1}	b_{A0} Pa^{-1}	E_A kJ mol^{-1}	$q_{B,sat}$ mol kg^{-1}	b_{B0} Pa^{-1}	E_B kJ mol^{-1}
C_2H_2	1.4	3.536E-15	56	2.45	2.809E-13	54
CO_2	0.12	6.138E-07	12.6	2.5	1.218E-14	52

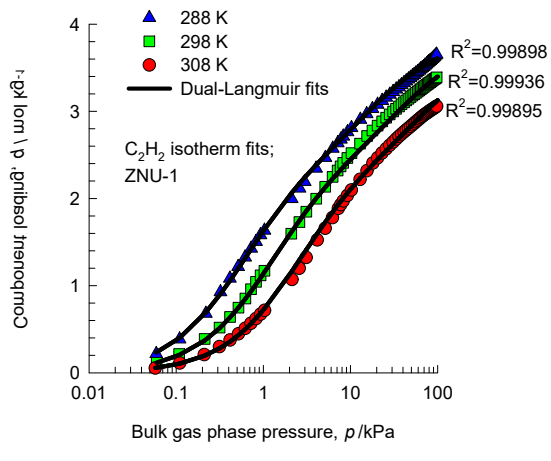

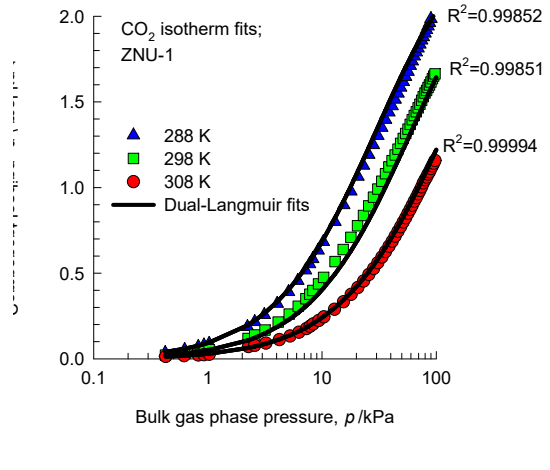

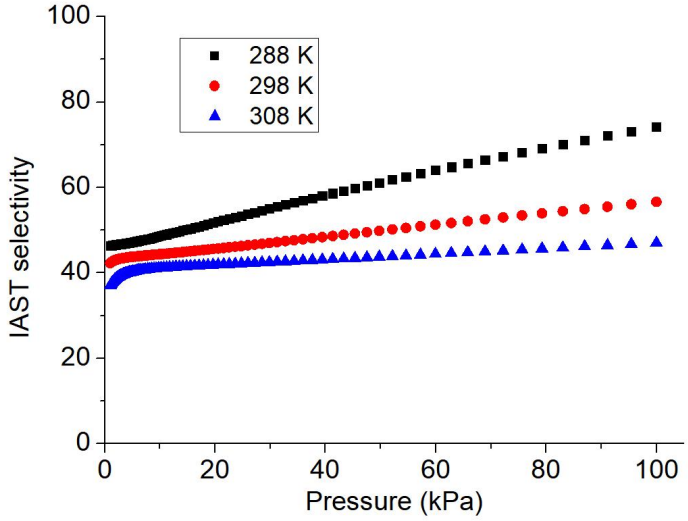

Figure S15. IAST selectivity of ZNU-1 towards a gas mixture of C_2H_2/CO_2 (50/50) at 288, 298, and 308 K.

The IAST selectivity at 288 K was 46.3-74.2 under the pressure range of 1-100 kPa.

The IAST selectivity at 298 K was 42.3-56.6 under the pressure range of 1-100 kPa.

The IAST selectivity at 308 K was 37.1-47.0 under the pressure range of 1-100 kPa.

The IAST selectivity was higher under lower temperature.

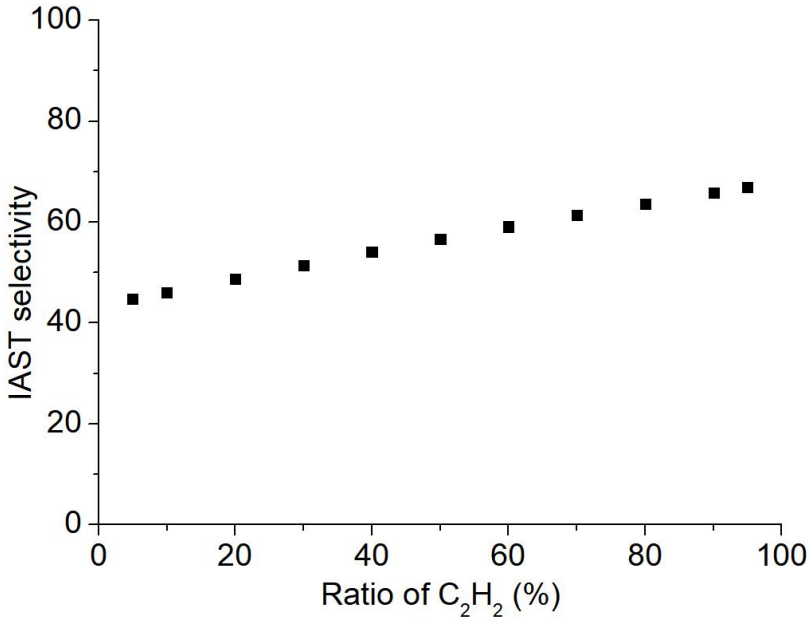

Figure S16. IAST selectivity of ZNU-1 towards a gas mixture of C_2H_2/CO_2 (50/50) at 298 K with different C_2H_2 ratio.

Table S4 Summary of the gas adsorption data of BSF-1, BSF-2, BSF-3, BSF-4, and ZNU-1

Materials		BSF-1	BSF-2	BSF-3	BSF-4	**ZNU-1**
C_2H_2 uptake at 298 K (mmol/g)	0.01 bar	0.14	0.14	0.77	0.52	**1.22**
	0.1 bar	0.94	0.82	2.29	1.44	**2.52**
	1 bar	2.35	1.85	3.59	2.38	**3.41**
CO_2 uptake at 298 K (mmol/g)	0.01 bar	0.035	0.026	0.20	0.04	**0.05**
	0.1 bar	0.30	0.21	1.03	0.37	**0.47**
	1 bar	1.77	1.33	2.11	1.60	**1.70**
C_2H_2/CO_2 (1:1) IAST selectivity	1-100 kPa	4.79-3.36	6.27-5.10	16.49-16.29	15.10-9.80	**42.3-56.6**
C_2H_2 Q_{st} (kJ/mol)		30.7	37.3	42.7	35.0	**54.0**
DFT calculated bonding energy of MOF and C_2H_2 (kJ/mol)		-35.7	-43.0	-41.8[a]	--	**-56.9**
CO_2 Q_{st} (kJ/mol)		21.7	28.7	25.5	24.5	**44.0**
DFT calculated bonding energy of MOF and CO_2 (kJ/mol)		-23.3	--	-28.1[a]	--	**-37.6**
BET surface area (m^2/g)		535	403	458	437	**532**

[a] Due to the large cell volume of BSF-3, only the dodecaborate pillars that are involved in the interaction with acetylene/carbon dioxide are isolated for calculation, therefore, the absolute values of the calculated bonding energies may be smaller than those with the consideration of the multiple Van der Waals interactions from the neutral organic ligands.

IV Breakthrough simulations and experiments

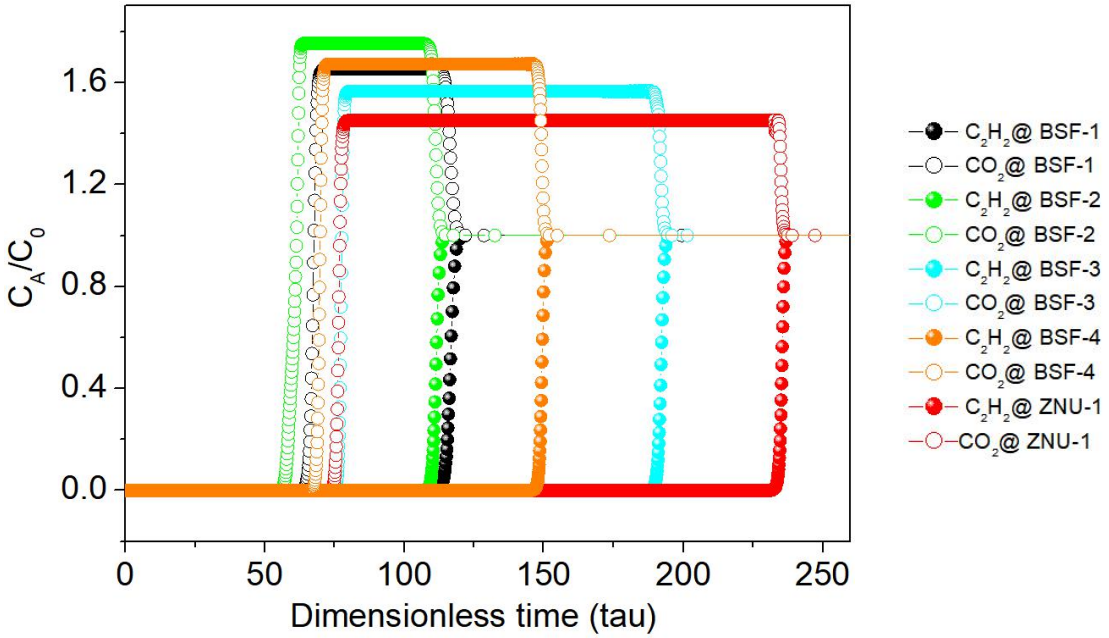

Figure S17. Simulated breakthrough curves for BSF-1, BSF-2, BSF-3, BSF-4 and ZNU-1 under the same conditions (length of packed bed, L = 0.3 m; voidage of packed bed, ε = 0.4; superficial gas velocity at inlet, u = 0.04 m/s. The x-axis is the *dimensionless* time tau, $\tau = t \times u / (L \times \varepsilon)$, defined by dividing the actual time, t, by the characteristic time, $L\varepsilon/u$. The materials with the same volume are used for comparison in the packed bed).

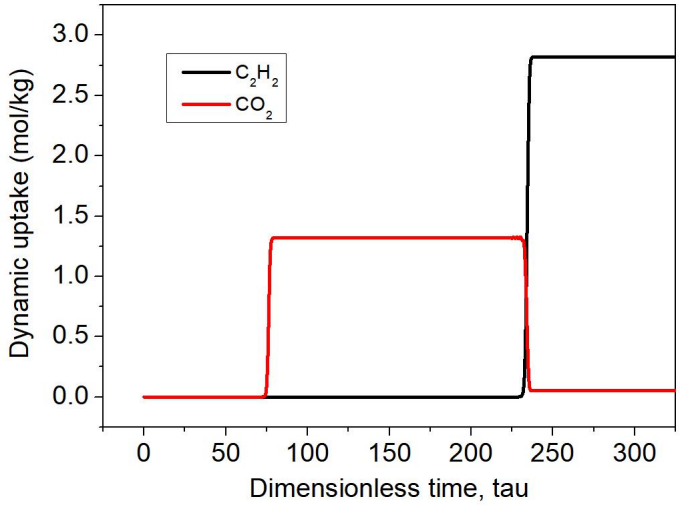

Figure S18. Simulated dynamic C_2H_2 and CO_2 uptake from the C_2H_2/CO_2 (50/50) mixture in ZNU-1.

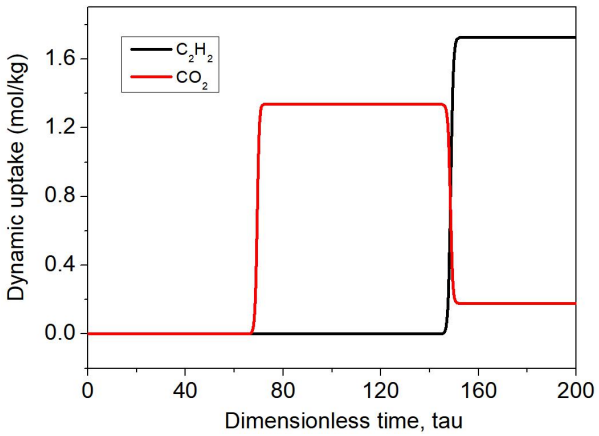

Figure S19. Simulated dynamic C_2H_2 and CO_2 uptake from the C_2H_2/CO_2 (50/50) mixture in BSF-4.

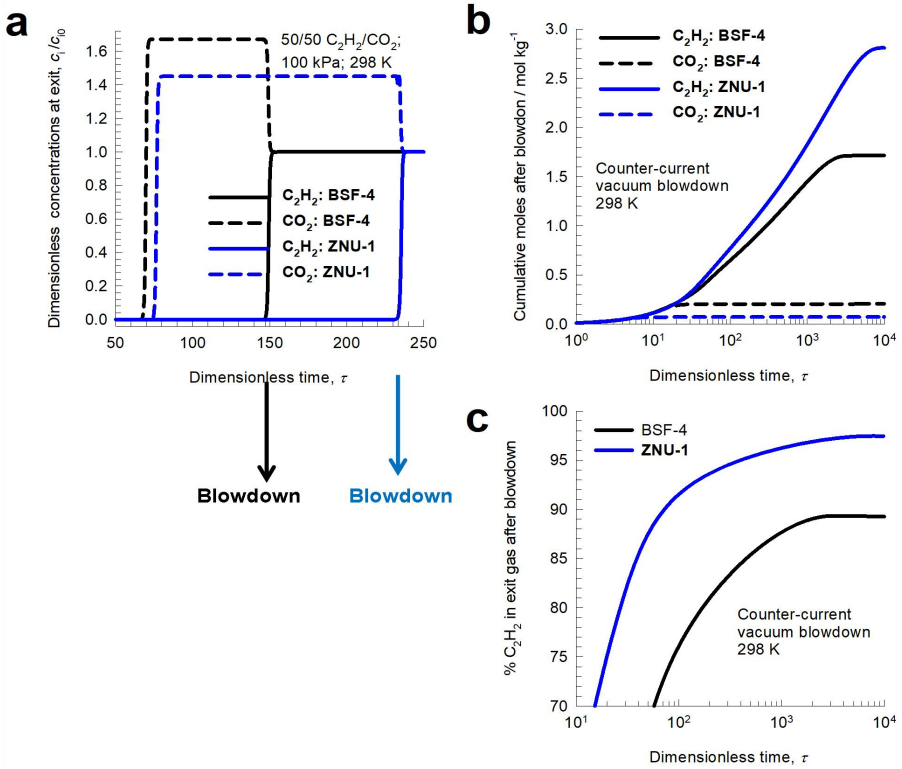

Figure S20. (a) Simulations of transient breakthroughs of $C_2H_2(1)/CO_2(2)$ mixtures in fixed bed packed with ZNU-1 and BSF-4 operating at 298 K and 100 kPa with feed compositions $y_{10} = y_{20} = 0.5$. (b) Simulations of counter-current blowdown operations. (c) Cumulative moles of $C_2H_2(1)$ and $CO_2(2)$ recovered during blowdown. (c) Purity of $C_2H_2(1)$ recovered during blowdown.

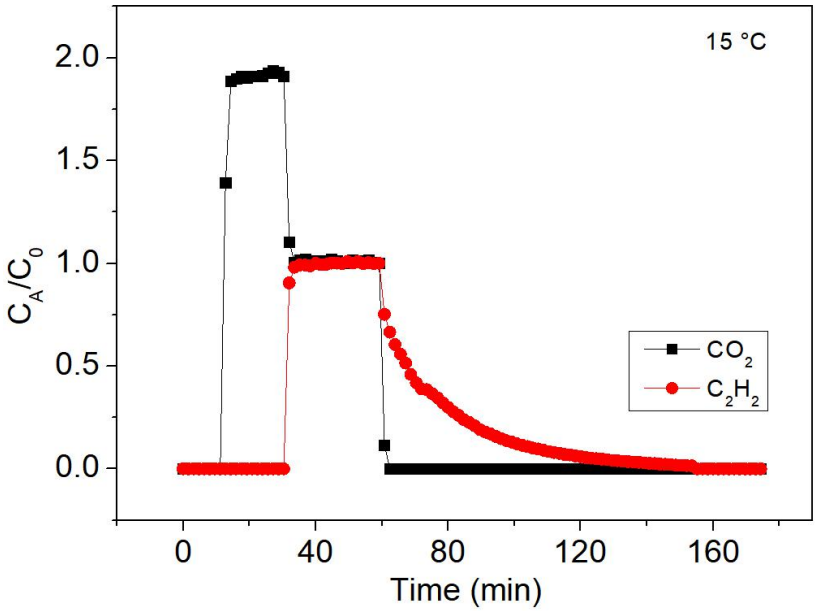

Figure S21. The experimental column (4.9 mm inner diameter × 100 mm length) breakthrough curves of ZNU-1 for C_2H_2/CO_2 (50/50) at 288 K with a flow rate of 5 mL/min and desorption curves (Ar, 5 mL/min, 348 K).

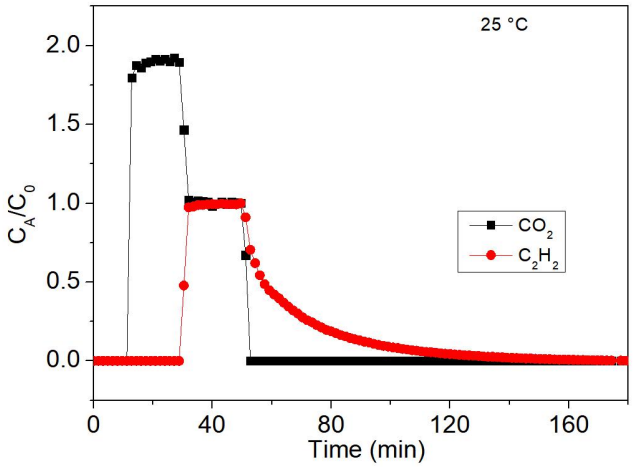

Figure S22. The experimental column (4.9 mm inner diameter × 100 mm length) breakthrough curves of ZNU-1 for C_2H_2/CO_2 (50/50) at 298 K with a flow rate of 5 mL/min and desorption curves (Ar, 5 mL/min, 348 K).

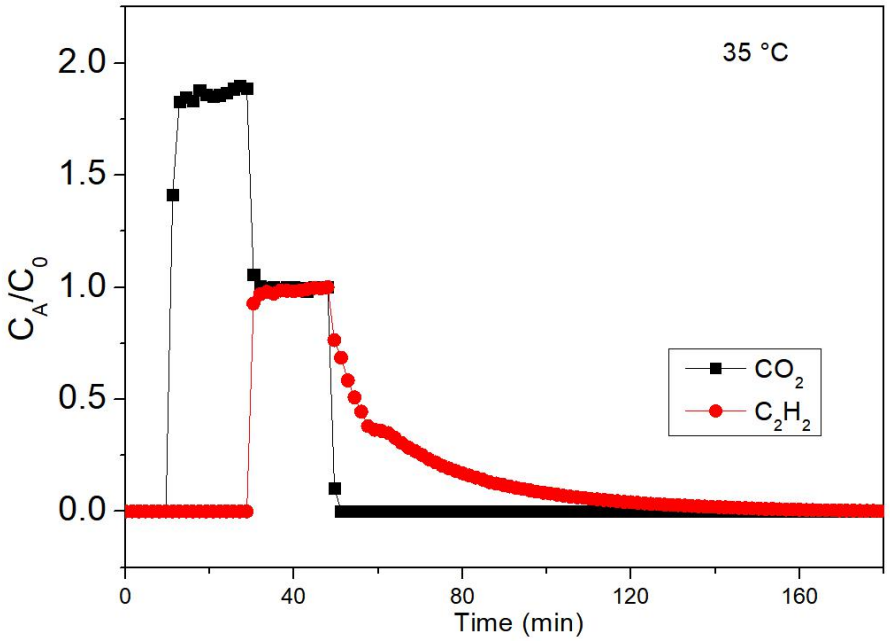

Figure S23. The experimental column (4.9 mm inner diameter × 100 mm length) breakthrough curves of ZNU-1 for C_2H_2/CO_2 (50/50) at 308 K with a flow rate of 5 mL/min and desorption curves (Ar, 5 mL/min, 348 K).

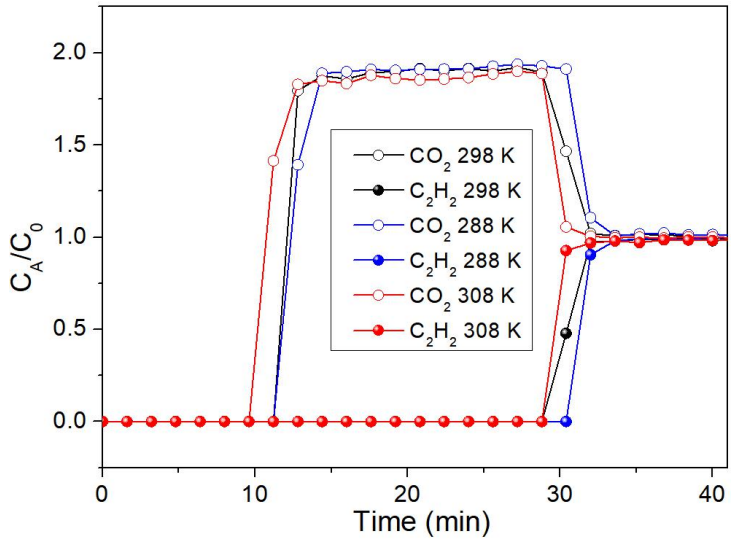

Figure S24. Comparison of the experimental column (4.9 mm inner diameter × 100 mm length) breakthrough curves of ZNU-1 for C_2H_2/CO_2 (50/50) at 288, 298 and 308 K.

Table S5 Summary of column (4.9 mm inner diameter × 100 length) breakthrough time of CO_2 and C_2H_2 in ZNU-1

	288 K	298 K	308 K
CO_2	12.8 min	12.8 min	11.2 min
C_2H_2	32.0 min	30.4 min	30.4 min

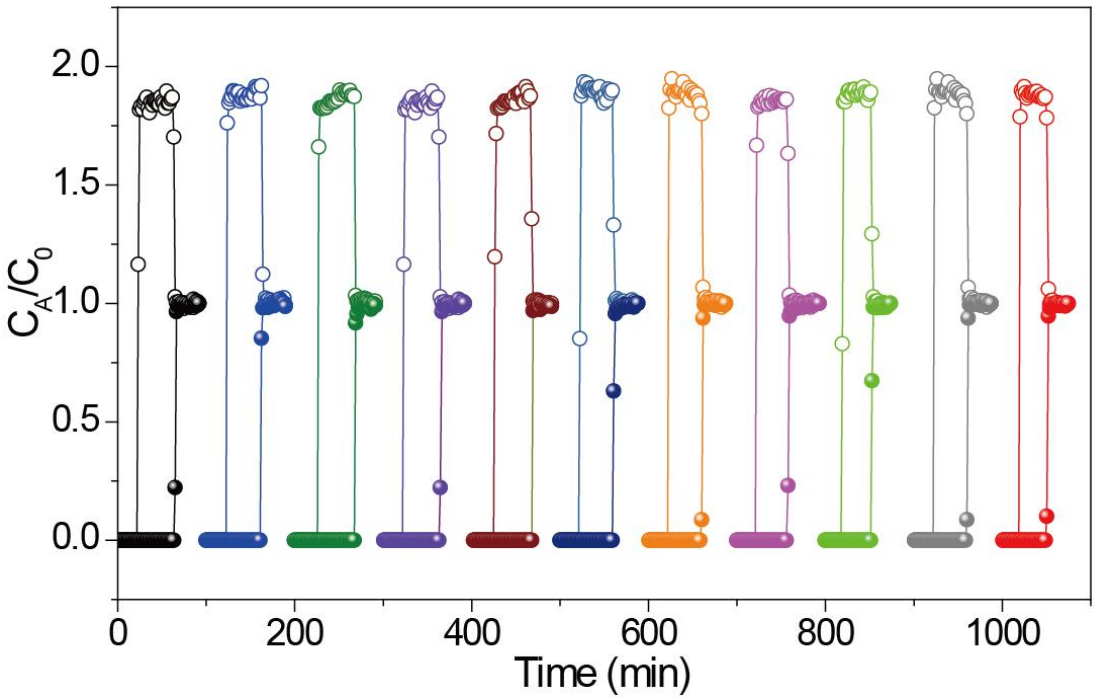

Figure S25. The experimental column (5 mm inner diameter × 200 mm length) breakthrough curves of ZNU-1 for C_2H_2/CO_2 (50/50) at 298 K with a flow rate of 5 mL/min over 10 cycles.

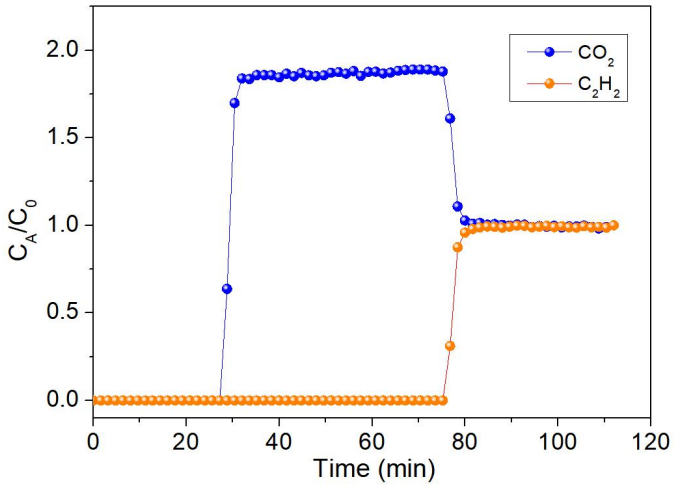

Figure S26. The experimental column (5 mm inner diameter × 200 mm length) breakthrough curves of ZNU-1 for C_2H_2/CO_2 (50/50) at 298 K with a flow rate of ~3.5 mL/min.

V DFT Calculation & GCMC simulation

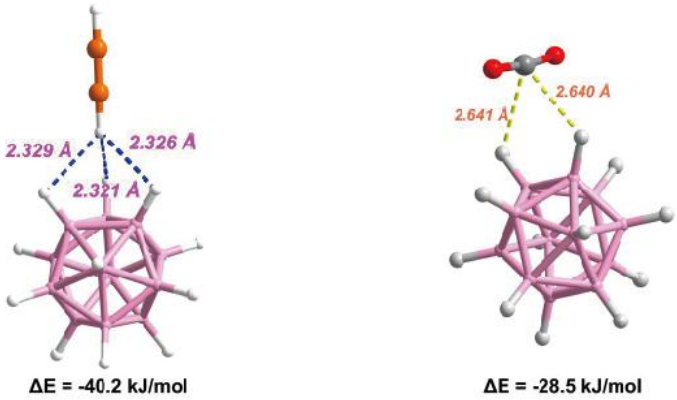

Figure S27. DFT calculated binding energy between one dodecaborate and C_2H_2, C_2H_4 or CO_2.

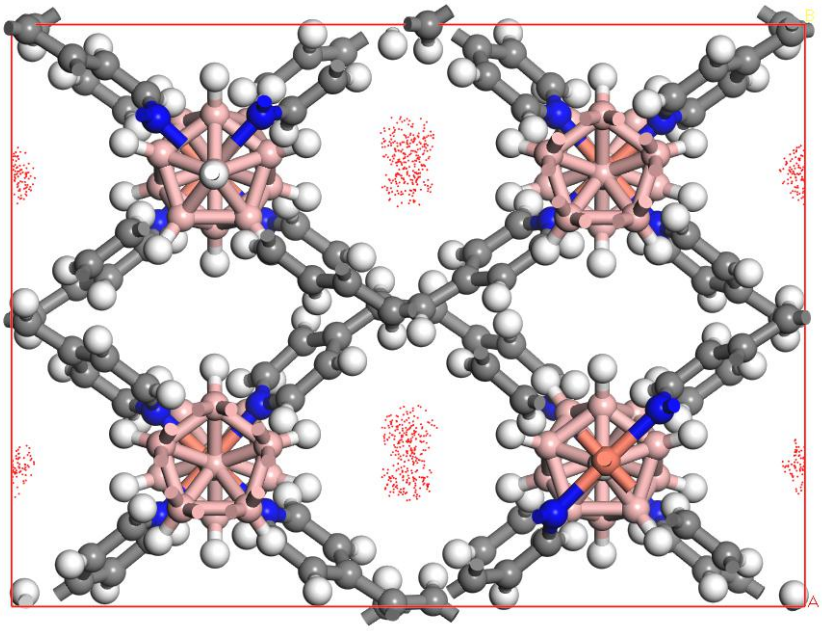

Figure S28. GCMC simulated C_2H_2 adsorption sites in ZNU-1.

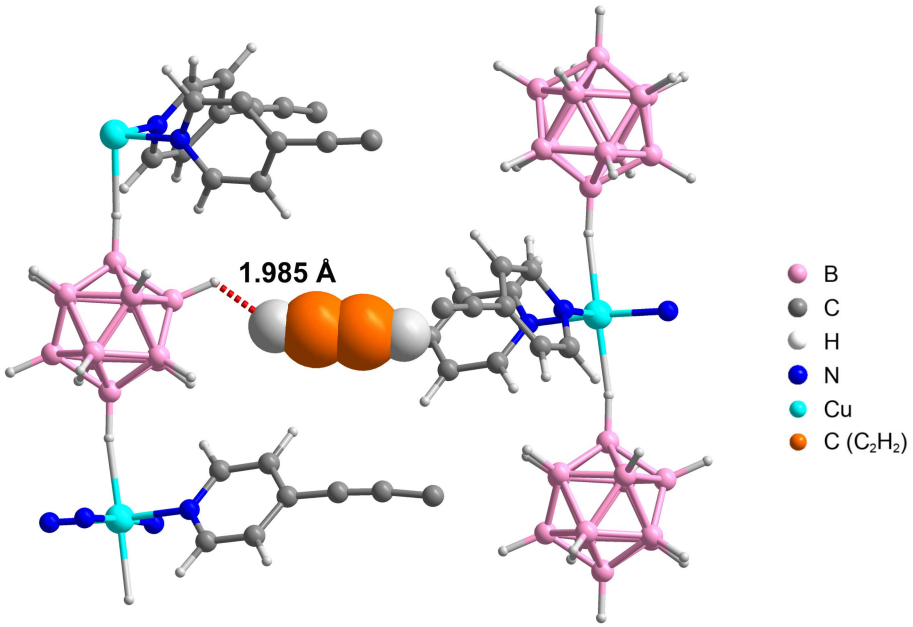

Figure S29. The DFT-D optimized adsorption configuration of C_2H_2 in BSF-1. Only single B-$H^{\delta-}\cdots H^{\delta+}$-C≡C-$H^{\delta+}$ bonds (1.985 Å) was observed.

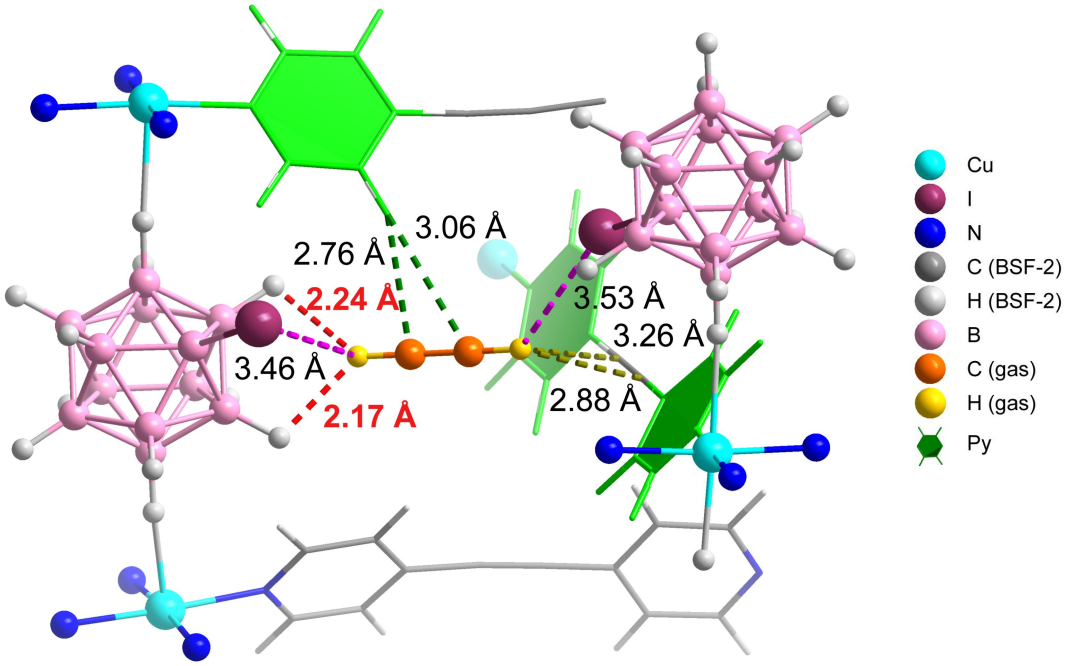

Figure S30. The DFT-D optimized adsorption configuration of C_2H_2 in BSF-2. Two B-$H^{\delta-}\cdots H^{\delta+}$-C≡C-$H^{\delta+}$ bonds (2.24, 2.17 Å) at single site was observed.

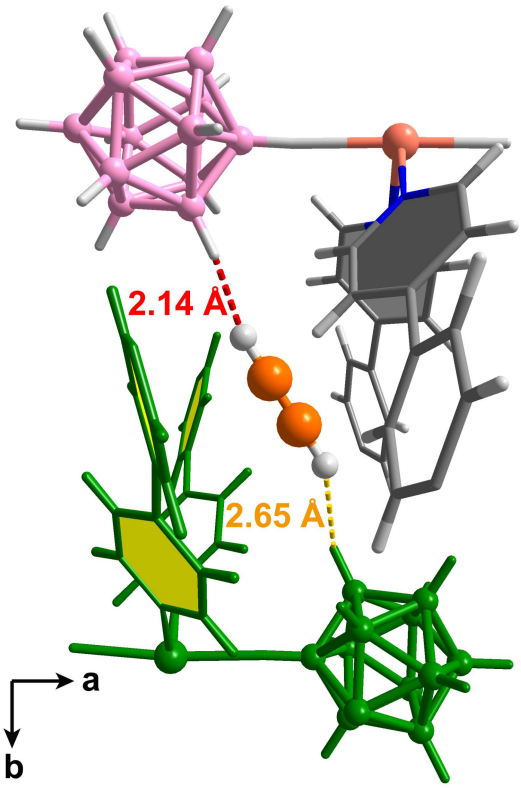

Figure S31. The GCMC optimized adsorption configuration of C_2H_2 in BSF-3. Only single B-$H^{\delta-}\cdots H^{\delta+}$-C≡C-$H^{\delta+}$ bond (2.14 Å) was observed.

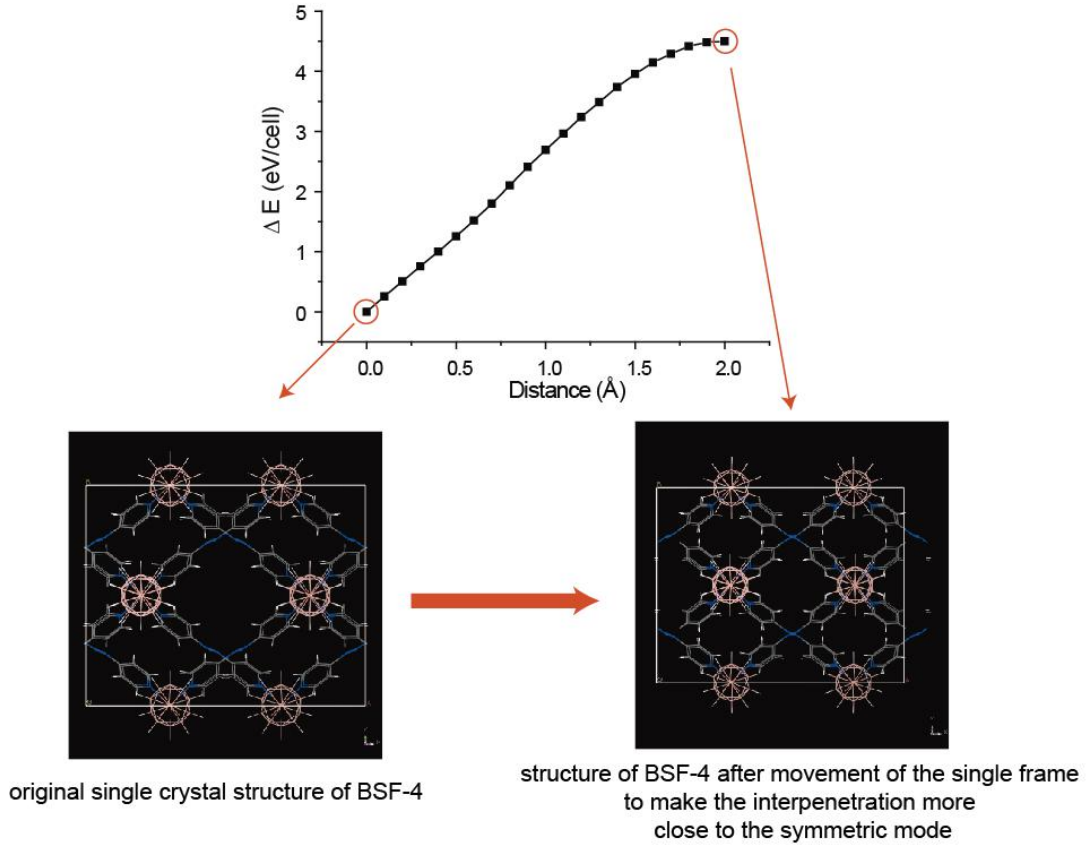

Figure S32. The DFT calculated energy change of BSF-4 with the movement of single net. From the calculated results, the original BSF-4 is most likely to be the thermodynamic product.

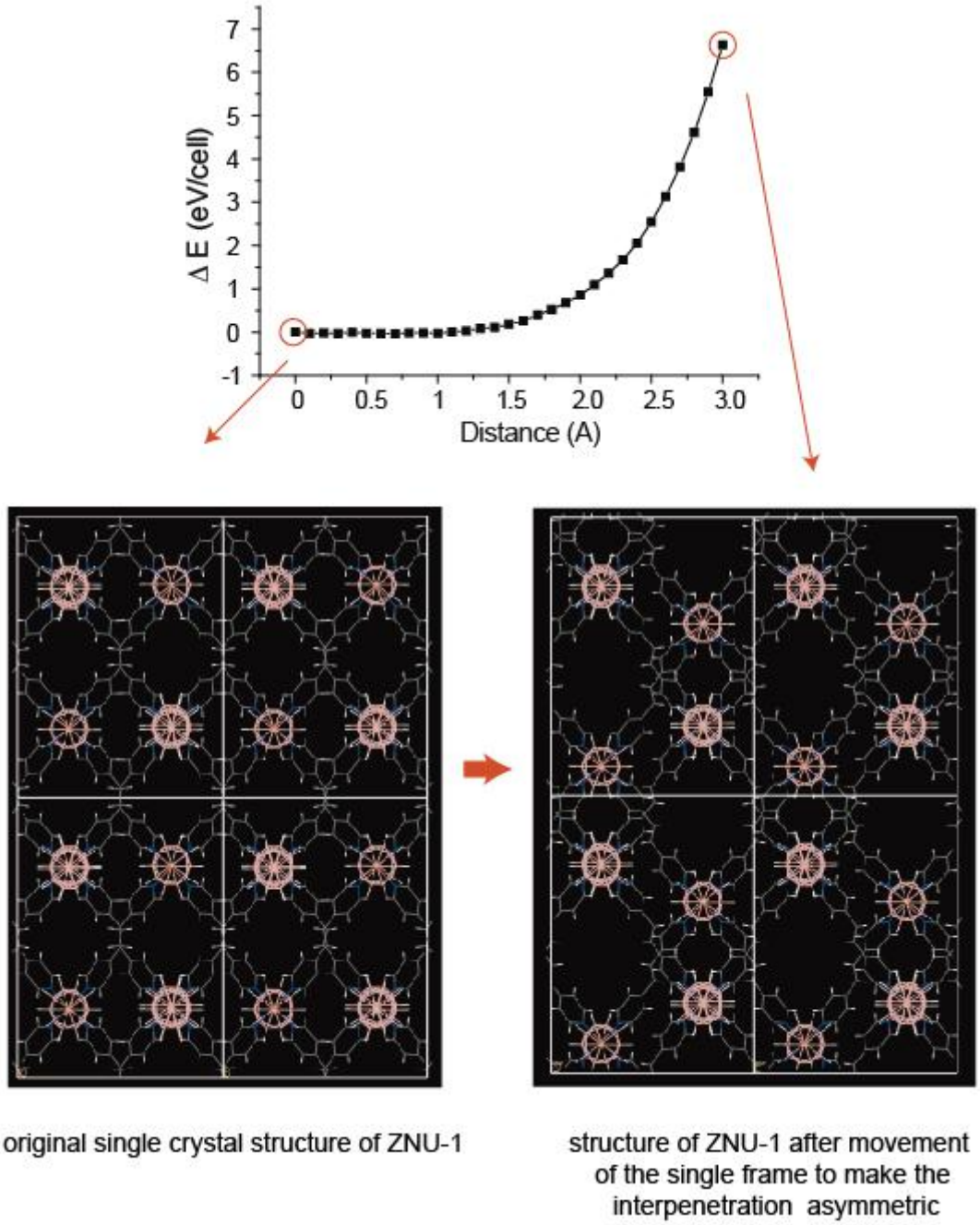

Figure S33. The DFT calculated energy change of ZNU-1 with the movement of single framework. From the calculated results, there was negligible energy difference between the original framework ZNU-1 and the simulated framework after the movement of single net within 1 Å. With further movement of the net, the structure will be less stable. After having a closer look at differences in energies, it seems that the structures after movement between 0.1-1 Å was even slightly more stable. Therefore, we think the original ZNU-1 is likely to be the product controlled both by thermodynamics and kinetics.

VI Additional kinetic gas adsorption data

To further understand the gas adsorption behavior in ZNU-1, pure component kinetic data was collected every 3 seconds on the Autosorb iQ instrument under the mode of "Vector Dose". The pressure range was chosen as 0-0.6 bar and the equilibrium time is 2 s. Based on the static gas adsorption isotherms, the vector dose for C_2H_2 was set as 0.0481 g × 71 cc/g (adsorption capacity under 0.5 bar) = 3.4 cc; for CO_2 was set as 0.0481 g × 29 cc/g (adsorption capacity under 0.5 bar) = 1.4 cc. The adsorption isotherms of C_2H_2 under "Vector Dose" mode was shown in Figure S33. The kinetic data under the pressure of 0.04641, 0.14216, 0.25328, 0.36873, and 0.48588 bar were shown in Figure S34. The adsorption isotherms of CO_2 under "Vector Dose" mode was shown in Figure S35. The kinetic data under the pressure of 0.04041, 0.08281, 0.12578, 0.16967, and 0.21425 bar were shown in Figure S36. The analysis was complete within 89 minutes for C_2H_2 and 47 minutes for CO_2. Having a closer look at the first five collecting points, the time used for reaching C_2H_2 adsorption saturation under the corresponding pressures were ~630, 324, 255, 201 and 178 seconds while it is ~582, 129, 126, 126 and 126 seconds for CO_2. Therefore, the adsorption kinetic for CO_2 is faster than that for C_2H_2 while both are relatively fast. This could be explained by the stronger interactions between ZNU-1 and C_2H_2 that hinders the gas diffusion inside the channel.

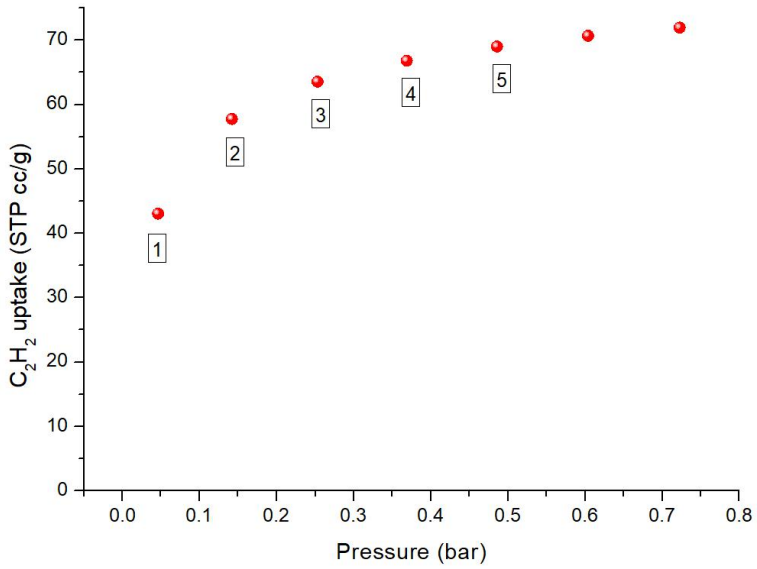

Figure S34. C_2H_2 adsorption isotherms under 298 K measured under mode of "Vector Dose".

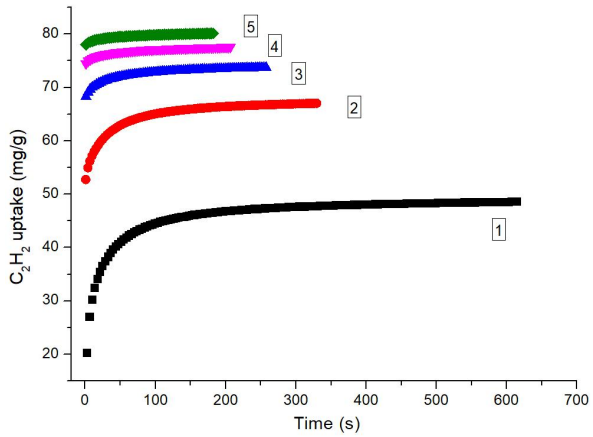

Figure S35. Kinetic C_2H_2 adsorption data under 298 K under the pressure of 0.04641, 0.14216, 0.25328, 0.36873, 0.48588 bar. The time used for reaching C_2H_2 adsorption saturation under the corresponding pressures was ~630, 324, 255, 201 and 178 seconds.

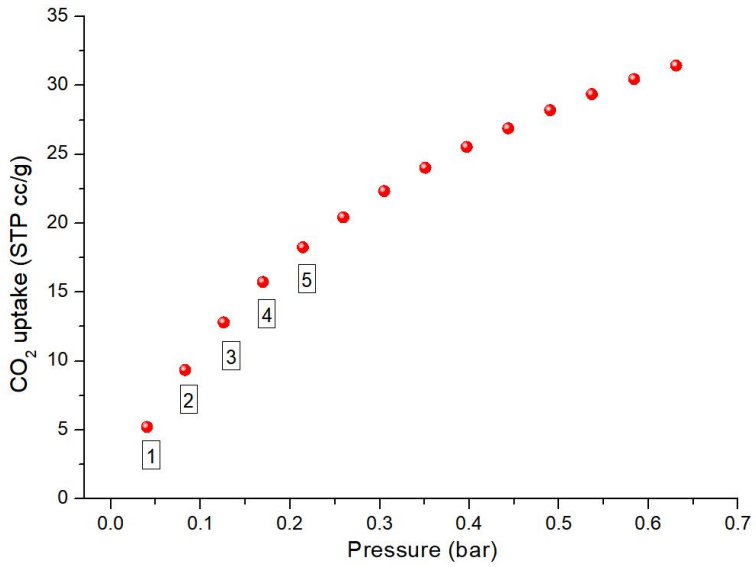

Figure S36. CO_2 adsorption isotherms under 298 K measured under mode of "Vector Dose".

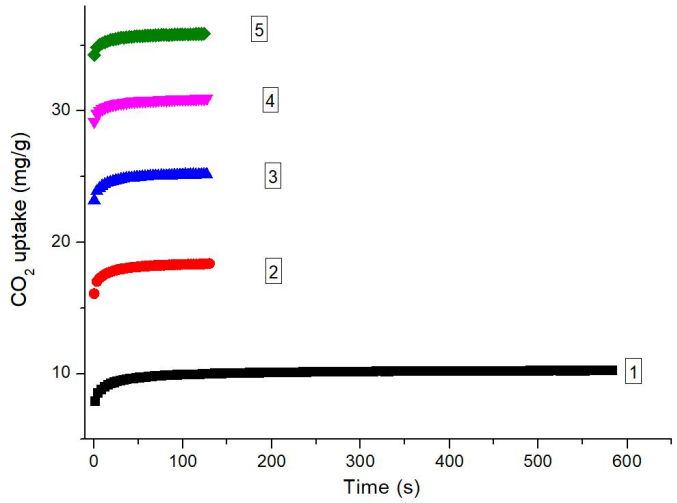

Figure S37. Kinetic CO_2 adsorption data under 298 K under the pressure of 0.04041, 0.08281, 0.12578, 0.16967, and 0.21425 bar. The time used for reaching CO_2 adsorption saturation under the corresponding pressures was ~582, 129, 126, 126 and 126 seconds.

VI Adsorption capacity/selectivity/Q_{st} comparison table

Table S6 Comparison of the reported materials on C_2H_2/CO_2 adsorption capacity, C_2H_2/CO_2 adsorption enthalpy (Q_{st}) and IAST selectivity towards C_2H_2/CO_2

Porous Materials	C_2H_2 uptake (cm^3/g)	CO_2 uptake (cm^3/g)	Q_{st} (C_2H_2) (kJ/mol)	Q_{st} (CO_2) (kJ/mol)	Selectivity	Ref
MOFs with molecular sieving effect						
CPL-1-NH_2	41.2	4.70	50.0	32.4	119	[1]
UTSA-300a	68.9	3.25	57.6	N.A.	743	[2]
MOFs with open metal sites						
UTSA-74a	107	71	31.7	25	9	[3]
JNU-1	63	51	13	24	3	[4]
SNNU-150-Al	97	44.4	29	24	7.27	[5]
PCP-33	121.8	58.6	27.5	26.2	6	[6]
ZJU-60	150	73.9	17.6	15.2	6.7[a]	[7]
NTU-54	22[c]	19[c]	38	35	3.8[c]	[8]
NTU-55	135.5	70	25	22	6.6[a]	[9]
Cu(BDC-Br)	34.3	24.2	26.1	25.6	3.9	[10]
NTU-66-Cu	111.5	49	32.3	21.7	6	[11]
SNNU-63	91.1	43.7	21.6	21.9	2.7	[12]
SNNU-65-Cu-Sc	178.9	70.4	44.9	22.2	13.5	[13]
SNNU-65-Cu-Fe	162.3	64.9	28.2	21.8	6.7	[13]
ZJU-199	128	62.4	38.5	19	4[b]	[14]
UTSA-68a	70.1	39.6	25.8	26	3.4[b]	[15]
ZJU-196a	83.5	8.5	39.2	N.A.	N.A.	[16]
UPC-200(Al)-F-BIM	144.5	55.5	20.5	14.2	3.15	[17]
FeNi-M ’MOF	96	60.9	27	24.5	24	[18]
NKMOF-1-Ni	61	51.1	60.3	40.9	26	[19]
SNNU-65	134	97.4	40	27.1	4.5	[20]

JXNU-5a	55.9	34.8	32.9	25.2	5	[21]
ZJU-74a	85.7	69	44.5	30	36.5	[22]
ATC-Cu	112.2		79.1		53.6	[23]
Cu@UiO-66-$(COOH)_2$	51.7	20	74.5	28.9	73*	[24]
MOFs without open metal sites						
$Cu_2(pzdc)_2(pyz)$	42[d]	4.6[d]	42.5	31.9	26[e]	[25]
JCM-1	75	38	36.9	33.4	13.7	[26]
FJU-36a	52.2	35.5	32.9	31.1	2.8	[27]
FJU-90a	180	103	25.1	20.7	4.3	[28]
ZJU-195a	214.2	105	29.9	20.7	4.7	[29]
UPC-110	73.4	24.3	24.6	16	5.1	[30]
ZJNU-13	118.4	87.9	33.5	22.5	5.64	[31]
MUF-17	67.4[f]	56.2[f]	49.5	33.8	6[f]	[32]
DICRO-4--Ni-i	43	23	37.7	33.9	13.9	[33]
$Ni_3(HCOO)_6$	94	68	40.9	24.5	22	[34]
TCuCl	67.2	44.8	41	30.1	16.9	[35]
TCuBr	62.7	44.8	36.8	26.8	9.5	[35]
TCuI	49.3	35.8	38.4	30.7	5.3	[35]
ZJUT-2	76[b]	49[b]	41.5	31.5	10[b]	[36]
TIFSIX-2-Ni-i	94.3	101.6	40	34	6.1	[37]
BSF-1	52.5	39.7	30.7	21.7	3.4	[38]
BSF-2	41.5	29.7	37.3	28.7	5.1	[39]
BSF-3	79.7	47.3	42.7	25.5	16.3	[40]
BSF-4	53.2	35.8	35.0	24.5	9.8	[41]
ZNU-1	**76.3**	**38.1**	**54.0**	**44.0**	**56.6**	**This work**
	82.5[g]	**46.7[g]**			**74.2[g]**	
	69.1[h]	**26.7[h]**			**47.0[h]**	

[a] IAST selectivity at 0.15 bar for 1 : 1 (v/v) C_2H_2/CO_2. [b] At 296 K. [c] At 273 K. [d] At 270 K. [e] Uptake ratio at 0.01 bar and 270 K. [f] At 293 K. [g] at 288 K. [h] at 308 K

N. A. = not available.

* The reported value of 185 in Ref 24 is a mistake. 185 is the IAST selectivity under 273 K (see Figure S29 in Ref. 24) while the IAST selectivity for C_2H_2/CO_2 (1/1) at 298 K is ~73

[1] L. Yang, L. Yan, Y. Wang, Z. Liu, J. He, Q. Fu, D. Fu, D. Liu, X. Gu, P. Dai, L. Li, X. Zhao, *Angew. Chem. Int. Ed*., **2021**, *60*, 4570–4574.

[2] R. B. Lin, L. B. Li, H. Wu, H. Arman, B. Li, R. G. Lin, W. Zhou, B. Chen, *J. Am. Chem. Soc.*, **2017**, 139, 8022–8028.

[3] F. Luo, C. S. Yan, L. L. Dang, R. Krishna, W. Zhou, H. Wu, X. L. Dong, Y. Han, T. L. Hu, M. O'Keeffe, L. L. Wang, M. B. Luo, R. B. Lin, L. Chen, *J. Am. Chem. Soc.*, **2016**, *138*, 5678–5684.

[4] H. Zeng, M. Xie, Y. L. Huang, Y. F. Zhao, X. J. Xie, J. P. Bai, M. Y. Wan, R. Krishna, W. G. Lu, D. Li, *Angew. Chem. Int. Ed.,* **2019**, 58, 8515–8519.

[5] H. J. Lv, Y. P. Li, Y. Y. Xue, Y. C. Jiang, S. N. Li, M. C. Hu, Q. G. Zhai, *Inorg. Chem.*, **2020**, *59*, 4825–4834.

[6] J. G. Duan, W. Q. Jin, R. Krishna, *Inorg. Chem*., **2015**, 54, 4279–4284.

[7] X. Duan, Q. Zhang, J. F. Cai, Y. Yang, Y. J. Cui, Y. B. He, C. D. Wu, R. Krishna, L. Chen, G. D. Qian, *J. Mater. Chem. A*, **2014**, *2*, 2628–2633.

[8] S. Liu, Y. H. Huang, Q. B. Dong, H. J. Wang, J. G. Duan, *Inorg. Chem*., **2020**, 59, 9569–9578.

[9] Q. B. Dong, Y. N. Guo, H. F. Cao, S. N. Wang, R. Matsuda, J. G. Duan, *ACS Appl. Mater. Interfaces*, **2020**, 12, 3764–3772.

[10] H. Cui, Y. X. Ye, H. Arman, Z. Q. Li, A. Alsalme, R. B. Lin, L. Chen, *Cryst. Growth Des.*, **2019**, *19*, 5829–5835.

[11] S. Chen, N. Behera, C. Yang, Q. B. Dong, B. S. Zheng, Y. Y. Li, Q. Tang, Z. X. Wang, Y. Q. Wang, J. G. Duan, *Nano Res*., **2020**, DOI: 10.1007/s12274-020-2935-1.

[12] Y. T. Li, J. W. Zhang, H. J. Lv, M. C. Hu, S. N. Li, Y. C. Jiang, Q. G. Zhai, *Inorg. Chem*., **2020**, 59, 10368–10373.

[13] J. W. Zhang, M. C. Hu, S. N. Li, Y. C. Jiang, P. Qu, Q. G. Zhai, *Chem. Commun*., **2018**, 54, 2012–2015.

[14] L. Zhang, C. Zou, M. Zhao, K. Jiang, R. B. Lin, Y. B. He, C. D. Wu, Y. J. Cui, B. Chen, G. D. Qian, *Cryst. Growth Des*., **2016**, 16, 7194–7197.

[15] G. G. Chang, B. Li, H. L. Wang, T. L. Hu, Z. B. Bao, B. Chen, *Chem. Commun*., **2016**, 52, 3494–3496.

[16] L. Zhang, K. Jiang, L. B. Li, Y. P. Xia, T. L. Hu, Y. Yang, Y. J. Cui, B. Li, B. Chen, G. D. Qian, *Chem. Commun*., **2018**, *54*, 4846–4849.

[17] W. D. Fan, S. Yuan, W. J. Wang, L. Feng, X. P. Liu, X. R. Zhang, X. Wang, Z. X. Kang, F. N. Dai, D. Q. Yuan, D. F. Sun, H. C. Zhou, *J. Am. Chem. Soc*., **2020**, *142*, 8728–8737.

[18] J. K. Gao, X. F. Qian, R. B. Lin, R. Krishna, H. Wu, W. Zhou, B. Chen, *Angew. Chem*., **2020**, 59, 4396–4400.

[19] Y. L. Peng, T. Pham, P. F. Li, T. Wang, Y. Chen, K. J. Chen, K. A. Forrest, B. Space, P. Cheng, M. J. Zaworotko, Z. J. Zhang, *Angew. Chem., Int. Ed*., **2018**, 57, 10971–10975.

[20] Y. P. Li, Y. Wang, Y. Y. Xue, H. P. Li, Q. G. Zhai, S. N. Li, Y. C. Jiang, M. C. Hu, X. H. Bu, *Angew. Chem., Int. Ed*., **2019**, *58*, 13590–13595.

[21] R. Liu, Q. Y. Liu, R. Krishna, W. J. Wang, C. T. He, Y. L. Wang, *Inorg. Chem*., **2019**, *58*, 5089–5095.

[22] J. Pei, K. Shao, J. X. Wang, H.-M. Wen, Y. Yang, Y. Cui, R. Krishna, B. Li, G. D. Qian, *Adv. Mater.*, **2020**, *32*, 1908275.

[23] Z. Niu, X. Cui, T. Pham, G. Verma, P. C. Lan, C. Shan, H. Xing, K. A. Forrest, S. Suepaul, B. Space, A. Nafady, A. M. Al-Enizi, S. Ma, *Angew. Chem. Int. Ed*. **2021**, *60*, 5283–5288.

[24] L. Zhang, K. Jiang, L.Yang, L. Li, E. Hu, L.Yang, K. Shao, H. Xing, Y. Cui, Y. Yang, B. Li, B. Chen, G. Qian, *Angew. Chem. Int. Ed*., **2021**,10.1002/anie.202102810.

[25] R. Matsuda, R. Kitaura, S. Kitagawa, Y. Kubota, R. V. Belosludov, T. C. Kobayashi, H. Sakamoto, T. Chiba, M. Takata, Y. Kawazoe, Y. Mita, Nature, 2005, 436, 238–241.

[26] J. Lee, C. Y. Chuah, J. Kim, Y. Kim, N. Ko, Y. Seo, K. Kim, T. H. Bae, E. Lee, *Angew. Chem. Int. Ed.*, **2018**, *57*, 7869–7873.

[27] L. Z. Liu, Z. Z. Yao, Y. X. Ye, L. J. Chen, Q. J. Lin, Y. S. Yang, Z. J. Zhang, S. C. Xiang, *Inorg. Chem.*, **2018**, *57*, 12961–12968.

[28] Y. X. Ye, Z. L. Ma, R. B. Lin, R. Krishna, W. Zhou, Q. J. Lin, Z. J. Zhang, S. C. Xiang,

B. Chen, *J. Am. Chem. Soc*., **2019**, *141*, 4130–4136.

[29] L. Zhang, K. Jiang, Y. P. Li, D. Zhao, Y. Yang, Y. J. Cui, B. Chen, G. D. Qian, *Cryst. Growth Des*., **2017**, *17*, 2319–2322.

[30] W. D. Fan, X. Wang, X. P. Liu, B. Xu, X. R. Zhang, W. J. Wang, X. K. Wang, Y. T. Wang, F. N. Dai, D. Q. Yuan, D. F. Sun, ACS Sustainable Chem. Eng., 2019, 7, 2134–2140.

[31] T. Xu, Z. Jiang, P. Liu, H. Chen, X. Lan, D. Chen, L. Li , Y. He, *ACS Appl. Nano Mater*., **2020**, *3*, 2911–2919.

[32] O. T. Qazvini, R. Babarao and S. G. Telfer, *Chem. Mater.*, **2019**, *31*, 4919–4926.

[33] H. S. Scott, M. Shivanna, A. Bajpai, D. G. Madden, K. J. Chen, T. Pham, K. A. Forrest, A. Hogan, B. Space, J. J. Perry, M. J. Zaworotko, *ACS Appl. Mater. Interfaces*, **2017**, *9*, 33395–33400.

[34] L. Zhang, K. Jiang, J. Zhang, J. Pei, K. Shao, Y. Cui, Y. Yang, B. Li, B. Chen, G. D. Qian, *ACS Sustainable Chem. Eng.* **2019**, *7*, 1667–1672.

[35] S. Mukherjee, Y. He, D. Franz, S. Q. Wang, W. R. Xian, A. A. Bezrukov, B. Space, Z. Xu, J. He, M. J. Zaworotko, *Chem. - Eur. J*., **2020**, *26*, 4923–4929.

[36] H. M. Wen, C. Liao, L. Li, L. Yang, J. Wang, L. Huang, B. Li, B. Chen, J. Hu, *Chem. Commun.*, **2019**, *55*, 11354–11357.

[37] M. Jiang, X. Cui, L. Yang, Q. Yang, Z. Zhang, Y. Yang, H. Xing, *Chem. Eng. J.* **2018**, *352*, 803–810.

[38] Y. Zhang, L. Yang, L. Wang, S. Duttwyler, H. Xing, *Angew. Chem. Int. Ed.* **2019**, *58*, 8145–8150.

[39] Y. Zhang, L. Yang, L. Wang, H. Xing, *J. Mater. Chem. A,* **2019**, *7*, 27560 –27566.

[40] Y. Zhang, J. Hu, R. Krishna, L. Wang, L. Yang, X. Cui, S. Duttwyler, H. Xing, *Angew. Chem. Int. Ed*., **2020**, *59*, 17664–17669.

[41] Y. Zhang L. Wang, J. Hu, S. Duttwyler, X. Cui, H. Xing, Solvent-dependent supramolecular self-assembly of boron cage pillared metal–organic frameworks for selective gas separation, *CrystEngComm*, **2020**, *22*, 2649–2655.